

Revision 2

1

2 **The relationship of destinezite to the acid sulfate alteration at the El Laco**
3 **magnetite deposit, Chile**

4

5 Francisco Velasco

6 Departamento de Mineralogía y Petrología, Facultad de Ciencia y Tecnología, E-48080

7 Bilbao, Spain francisco.velasco@ehu.es

8 Noelia De la Pinta

9 Departamentos de Física de la Materia Condensada y Física Aplicada, Facultad de
10 Ciencia y Tecnología, E-48080 Bilbao, Spain

11 Fernando Tornos

12 Instituto de Geociencias (IGEO, CSIC-UCM) – Doctor Severo Ochoa, 7, E-28040
13 Madrid, Spain

14 Thomas Briezewski

15 Departamentos de Física de la Materia Condensada y Física Aplicada, Facultad de
16 Ciencia y Tecnología, E-48080 Bilbao, Spain

17 Aitor Larrañaga

18 Sgiker Servicios Científicos, Universidad del País Vasco, Barrio Sarriena, s/n, E-48940
19 Leioa, Vizcaya, Spain

20

21 Corresponding author, e-mail: francisco.velasco@ehu.es

22 **Abstract**

23 Destinezite, ideally $\text{Fe}^{3+}_2(\text{PO}_4)(\text{SO}_4)(\text{OH})\cdot 6(\text{H}_2\text{O})$, is found as nodular lumps in hematite-
24 rich epiclastic sediments accumulated in small crater lakes on the slopes of El Laco
25 volcano. These lumps are almost entirely dominated by fine-grained destinezite
26 replacing earlier lipscombite, and associated with gray hematite. The crystal structure of
27 destinezite has been re-examined in order to test for possible differences with respect
28 to the earthy and poorly crystalline destinezite that forms by weathering in cave soils and
29 mine waste dumps. The structural refinements confirm that the differences found are
30 rather minor. The El Laco destinezite was refined in space group $P\bar{1}$ with $a = 9.5828(2)$,
31 $b = 9.7440(3)$, $c = 7.3302(3)$ Å, and $\alpha = 98.796(3)^\circ$, $\beta = 107.985(3)^\circ$, $\gamma = 63.898(2)^\circ$, $V =$
32 $584.50(4)$ Å³ and $Z = 1$. We measured by calorimetry the enthalpy and derived the
33 entropy and the Gibbs free energy of formation of destinezite (-4051.7 ± 4.3 kJ.mol⁻¹, $-$
34 1518.5 ± 20.0 kJ.mol⁻¹, -3598.9 ± 7.1 kJ.mol⁻¹, respectively). This has allowed us to
35 estimate the equilibrium constant in the temperature range 0–300°C ($\log K = -27.97 \pm$
36 1.1). We can predict that destinezite coexists with hematite over the range of conditions
37 that typically encompass the steam-heated hydrothermal environments recognized at El
38 Laco. The presence of destinezite along with hematite and the occurrence of alunite,
39 jarosite and variscite in the system provide evidence of intense hydrothermal alteration
40 during the extrusion of Fe-rich melts at El Laco volcano. The mineral assemblage and
41 the available geochemical data suggest that destinezite formed in hydrothermal
42 conditions by “maturation” of an immiscible Fe–P-rich melt. An unknown Fe–P–O phase
43 produced by this melt was first replaced by lipscombite and later, owing to intense
44 sulfidation, by destinezite. This replacement took place in the vadose zone above the

45 paleowater table by relatively cool (<150°C) groundwaters acidified by oxidation of
46 magmatic SO₂ to aqueous sulfate in a steam-heated system. Our model precludes other
47 modes of formation, such as devitrification of hypothetical Fe–P–S–O-rich melts ejected
48 from the volcano and supergene crystallization.

49

50 Keywords: destinezite, acid-sulfate alteration, magnetite–apatite deposit, El Laco
51 volcano, Chile

52

53

54 Introduction

55 Destinezite and its partially amorphous equivalent, diadochite, both ideally
56 hydrated hydroxyphosphate-sulfates of ferric Fe, are rare minerals of the general
57 formula $\text{Fe}^{3+}_2(\text{PO}_4)(\text{SO}_4)(\text{OH})\cdot 6\text{H}_2\text{O}$ ([Matsubara et al., 1999](#); [Peacor et al., 1999](#);
58 [Naslund et al., 2002](#); [Lledó, 2005](#)). Generally, diadochite is partially amorphous,
59 whereas its polymorph destinezite is crystalline. They occur in cave soils, weathered
60 gossans and mine-waste dumps as poorly crystalline phases ([Peacor et al., 1999](#);
61 [Anthony et al., 2005](#)). Destinezite is the more common of the two owing to its clay-like
62 nature and its tendency to occur mixed in with other earthy minerals, such as delvauxite,
63 melanterite, rockbridgeite, phosphosiderite and “limonite” (names and formula of all
64 mentioned minerals in this text are in Table 1), which make its identification difficult.

65 Lumps of destinezite were first reported from El Laco by [Naslund et al. \(2002\)](#) as
66 clasts intermingled with unconsolidated “tephra”, part of the eruptive products of the
67 volcano. Some authors have suggested that they are pyroclastic fragments of an
68 immiscible Fe-P-S-rich magma erupted by the volcano ([Henríquez and Nyström, 1998](#);
69 [Lledó, 2005](#); [Naslund et al., 2009](#)). With this interpretation, these authors provided
70 support for the hypothesis that magnetite ores from El Laco represent crystallized Fe-
71 oxide melts ([Nystrom and Henríquez, 1994](#); [Naslund et al., 2002](#); [Lledó, 2005](#); [Mungall](#)
72 [et al., 2018](#)). As an alternative view, the supergene origin traditionally attributed to
73 destinezite–diadochite implies that they formed in direct contact with the atmosphere
74 and at room temperature ([Moiseeva, 1967, 1970](#); [Peacor et al., 1999](#)).

75 In this article, we describe the occurrence of destinezite and propose that it formed

76 during the advanced argillic alteration at the El Laco hydrothermal system. Whatever the
77 ultimate origin of the destinezite, it must have had an Fe-bearing phosphate precursor
78 that was transformed by sulfidation and hydration during a late low-temperature event.
79 The lack of thermodynamic properties necessary to test this interpretation prevents us
80 from determining whether the stability field of destinezite is compatible with that of the
81 assemblage of associated minerals and with the geochemical conditions of alteration.
82 We wish to acquire the thermodynamic data considered essential to discuss the origin of
83 the El Laco destinezite, chiefly enthalpy, entropy, and its Gibbs free energy of formation.
84 This research provides new information on destinezite, in particular its chemical
85 composition, its degree of crystallinity, and some aspects of crystal structure. The study
86 also provides insights about the process of transformation of the identified phosphate
87 precursor, based on the stability fields of the mineral phases involved.

88 **Geological background**

89 The El Laco Fe deposit is located in the active Cenozoic volcanic arc of the Andes
90 near the Chile–Argentina border, at 4800–5200 meters above sea level (Fig. 1). Four
91 volcanic units dominated by flows have been recognized in the area ([Velasco et al.,](#)
92 [2016](#)). Perhaps the most intriguing feature is the presence of stratabound bodies of
93 magnetite at or near the contact between the Lower and Upper Andesite units. A
94 younger generation of later andesite flows, volumetrically less important, is found near
95 the principal vent. Andesite belonging to the Upper and Lower units have high content of
96 magnetite, mainly occurring as small microphenocrysts in the volcanic groundmass. It
97 also contains small crystals of apatite, both disseminated in the groundmass and
98 included in the pyroxene phenocrysts ([Velasco et al., 2016](#); [Tornos et al., 2017](#)).

99 The deposit comprises seven ore bodies of massive magnetite within a 8 x 4 km²
100 area, with estimated resources of about 750 Mt of ore grading about 60% Fe ([Naslund et](#)
101 [al., 2002](#); [Tornos et al., 2016, 2017](#)). Magnetite ore bodies form a semicircle around an
102 andesitic plug; their location may be controlled by a caldera collapse structure (Fig. 1)
103 ([Keller et al., 2018](#)). They occur either as subvertical dikes or as related larger strata
104 bound bodies, linked invariably to a recognizable feeder structure. These magnetite ore
105 bodies resemble edifices typical of basaltic shield volcanoes and include dome- or cone-
106 like morphologies, having associated lava-lake infillings and volcanoclastic deposits
107 ([Nystrom and Henríquez, 1994](#); [Tornos et al., 2017](#)). Crosscutting the whole magnetite
108 lenses are abundant but discontinuous tubes coated with skeletal clinopyroxene and
109 euhedral magnetite with unidirectional growth structures. Tubes and, to a lesser extent,
110 abundant vesicles, are irregularly coated by products of hydrothermal activity such as
111 quartz, sanidine, alunite, hematite, Fe-bearing phosphates, and fluorite.

112 Magnetite is the dominant mineral in the large stratabound orebodies, but it has
113 been widely replaced by maghemite, and this transformed to hematite in zones that
114 underwent pervasive hydrothermal alteration. Most of the magnetite is characteristically
115 Ti-poor, with TiO₂ contents lower than 0.1 wt%, and trace amounts of Cr, V, and Ni
116 ([Dare et al., 2015](#); [Velasco et al., 2016](#); [Broughm et al., 2017](#)). Apatite, largely
117 fluorapatite, is locally abundant and may reach up to 10 vol.% in the feeder structures. In
118 the stratabound bodies, it is fairly common to find it lining cavities or nucleating along
119 intrusive contacts ([Henriquez and Martin, 1978](#)).

120 Regional mapping, geochemistry, and petrography show that there are several
121 superimposed stages of hydrothermal activity ([Rhodes et al., 1999](#); [Naranjo et al., 2010](#);

122 [Velasco and Tornos, 2012](#); [Tornos et al., 2016, 2017](#)). In deep areas beneath the
123 stratabound ores, the andesite has undergone pervasive high-temperature alkali-calcic
124 alteration. Both phenocrysts and groundmass are replaced by diopside, adularia, a
125 scapolite-group mineral, magnetite and anhydrite. At shallow depth, the alteration
126 resulted in strong bleaching of the andesite owing to pervasive replacement by alunite
127 and to the leaching of Fe associated with the advanced argillic alteration of the rocks
128 (Fig. 1A, 1B). This alteration was mainly controlled by northwest-southeast faults. The
129 resulting assemblages consist of fine-grained alunite exhibiting a pseudocubic habit
130 (rhombohedral crystals with nearly cubic angles), kaolinite, smectite, gypsum, tridymite,
131 jarosite, variscite, fluorite and, more rarely, pyrite and chalcopyrite. Most of the hematite
132 occurs as a pseudomorph after magnetite but locally appears as coarse-grained
133 euhedral to subhedral crystals replacing magnetite and disseminated in the altered
134 andesite.

135 The ore bodies, especially at Laco Sur, are commonly brecciated, with fragments
136 of the altered host andesite supported by massive magnetite ([Henriquez and Martin,
137 1978](#); [Nystrom and Henríquez, 1994](#); [Naslund et al., 2002](#); [Henriquez et al., 2003](#);
138 [Nystrom et al., 2016](#); [Ovalle et al., 2018](#)). These exposures have been recently
139 interpreted as being part of small diatreme–maar complexes ([Tornos et al., 2016, 2017](#)).
140 These complexes end up in crater lakes that are infilled by alluvial fan and fluvio-glacial
141 sediments made up almost exclusively of hematite. In some instances, they are covered
142 by later structureless eluvial gravel and silt. The hematite shows a well-defined parallel
143 but discontinuous layering, with poorly sorted grain-size distribution and local erosional
144 bottoms, all of them indicative of traction in a subaqueous environment. These hematite-

145 rich deposits have been interpreted as variably reworked and altered pyroclastic ejecta
146 coeval with the steam-rich extrusion of the Fe-rich melts ([Tornos et al., 2017](#)).

147 Within the hematite-rich sediments (Fig. 2), abundant angular clasts or irregular
148 compact lumps (nodules) up to 15 cm in diameter are composed mainly of destinezite.
149 Its characteristic orange color contrasts with the dark gray groundmass ([Naslund et al.,
150 2003](#); [Lledó, 2005](#); [Naslund et al., 2009](#); [Nystrom et al., 2016](#); [Tornos et al., 2017](#)).
151 These lumps are found along some certain horizons (Fig. 2A, 2B). Interpretation of their
152 original morphology can be difficult because the nodules usually are broken and
153 scattered. In some cases, they preserve a bread crust structure and an unclear internal
154 lamination, and fractures similar to those found in juvenile pyroclastic fragments.
155 According to [Lledó \(2005\)](#) and [Naslund et al. \(2009\)](#), these lumps represent ejected
156 fragments of devitrified magma (bombs), which would explain why they usually present
157 a flat bottom, indicative of ductility when they impacted the ground. Most of the
158 destinezite aggregates have inclusions of hematite, mainly filling microfissures and, less
159 commonly, oxidized magnetite, grouped in nooks and crannies, and showing secondary
160 alteration. The intimate association of destinezite with hematite suggests that both
161 originated during the same process, prior to glacial erosion, transport, and
162 sedimentation, to form the overlying alluvial Holocene Fe-rich deposits.

163 **Materials and methods**

164 Twenty samples of destinezite were prepared and polished as standard thin
165 sections ready to be observed under the petrographic microscope in transmitted and
166 reflected light. After inspection to check for the presence of inclusions and

167 inhomogeneous zones, the cleanest samples were selected for the thermal study and
168 Rietveld refinement of X-ray diffraction data; those showing inclusions of magnetite or
169 hematite at the edge of grains or remnants of other minerals were rejected.

170 **X-ray diffraction analysis.** No single crystals of destinezite could be isolated for a
171 single-crystal study. Hence, several almost pure samples were powdered in an agate
172 mortar under ambient conditions to acquire powder X-ray diffraction patterns (XRD). The
173 scans were obtained using a Philips X-Pert PRO automated diffractometer with $\text{CuK}\alpha$
174 radiation ($\lambda=1.5418 \text{ \AA}$) and a PIXcel solid-state detector (active length in 2θ 3.347°) at
175 the General Research Services (SGIker) of the University of Basque Country, Leioa,
176 Spain), operated at 40 kV and 40 mA in theta–theta configuration, and fitted with a
177 diffracted-beam monochromator to filter out fluorescent X-rays. The samples were
178 mounted on a zero-background silicon wafer fixed in a generic sample holder. Data were
179 collected from 5 to 80° 2θ (step size = 0.026° and time per step = 4600 s) at room
180 temperature. A fixed divergence and antiscatter slit provided a constant volume of
181 sample illumination.

182 Removal of instrumental broadening was done by collecting a pattern for the LaB_6
183 standard at the same conditions and settings. The data obtained were fitted using the
184 Rietveld approach and the FullProf software ([Rodríguez-Carvajal, 2001](#)). For the
185 identification of phases in the powder mounts, we made use of the Powder Diffraction
186 File (PDF) database. We used the PANalytical X'Pert High Score program to index all
187 observed maxima. Run products from heating experiments were mounted on silicon
188 plates and analyzed with the same diffractometer (at room temperature), operated at 40

189 kV and 40 mA, using a continuous scan at increments of $0.026^\circ 2\theta$ and counting times
190 of 600 second per step.

191 The refinement of the structure of the representative sample (DiadoX-1A) was
192 performed in the space group $P\bar{1}$ using the parameters for destinezite described by
193 [Peacor et al. \(1999\)](#). To check the validity and to establish confidence in the results, we
194 collected five replicate patterns in order to minimize instrumental drift as well as short-
195 period fluctuations of the samples. The procedure did not require the removal of regions
196 shared by other foreign peak positions because of the absence of potential
197 contaminants. Consequently, we assumed that all the reflections are compatible with the
198 destinezite, and that no others reflections are present.

199 **Scanning Electron Microscopy (SEM).** The samples used for experiments were
200 characterized by scanning electron microscopy after coating with carbon using the
201 Schottky field emission (JEOL JSM-7000F) microscope at the SGIker Labs (University of
202 Basque Country). This unit ran at an accelerating voltage of 20 keV at a beam current in
203 the range 10–20 nA. The SEM images, results of energy-dispersive x-ray spectroscopy
204 analyses (EDS), and element-distribution patterns were used to characterize the
205 products.

206 **Electron-microprobe (EMP) analyses.** The chemical composition of selected
207 samples was investigated using the CAMEBAX electron microprobe (SGIker Labs) at an
208 accelerating voltage of 15 kV, with a current of 10 nA, a beam diameter of 2–3 μm , and
209 the following standards supplied by Spi Structure Probe Inc.: jadeite (Na), sanidine (K),
210 diopside (Ca), spodumene (Al, Si), hematite (Fe), olivine (Mg), apatite (P), alunite (S),

211 and pure metals (Mn, Cr, V, Ni, and Ti); the X-ray lines measured are $K\alpha$ in all cases.
212 Interferences between elements were minimized, and concentrations were corrected for
213 major-element matrix effects using the PAPmatrix correction procedure ([Pouchou and](#)
214 [Pichoir, 1984](#)). Detection limits were calculated with an accuracy of 2σ at the 95%
215 confidence level. At these conditions, the detection limits of all oxides was 0.01 wt.%,
216 and for minor and trace elements, it was better than 200-500 $\mu\text{g/g}$ depending on the
217 elements and settings.

218 **Calorimetric and thermogravimetric experiments.** Thermogravimetric measurements
219 (thermogravimetric and differential thermogravimetric analysis, TGA and DTG,
220 respectively) were performed on dry samples of “pure” destinezite (weight of samples
221 approx. 5–15 mg) on a TA Discovery series instrument over the temperature range 50–
222 900°C with a constant heating rate of 5°C/min, under a nitrogen atmosphere with a flow
223 rate of 20mL/min. Temperature calibration was performed under the same experimental
224 conditions using the Curie temperatures of nickel and aluminum as standards.
225 Differential scanning calorimetry (DSC) measurements were performed on the same
226 samples on SDT Q600 and DSC Q2000 TA calorimeter instruments, using heating rate
227 of 10°C/min under helium atmosphere (these equipment and lab facilities belong to the
228 Department of Applied Physics II, University of Basque Country, Leioa Spain). The DSC
229 samples were cut as small pieces with an approximate mass between 15-35 mg, and
230 then hermetically sealed in aluminum pans. For proper calibration of temperature and
231 heat flux was employed indium and sapphire as reference materials. Quantitative
232 DSC/DTG data obtained with the above instruments have allowed to calculate the ΔH
233 associated with each one of the seven stages of decomposition of the destinezite that

234 have been distinguished during the entire heating experiment (see Table 3). The
235 procedure assumes that the change in enthalpy per degree is equivalent to the heat
236 capacity of the material, at constant pressure, and may be measured by estimating the
237 area under the DSC curve between the temperature limits of each discriminated reaction
238 step. All the measures of DSC and TGA were coupled with other techniques, such as X-
239 ray diffraction and SEM-EDX, to provide an understanding of phase transitions, mainly
240 the characterization of the intermediate and final products formed at each heating stage.
241 After the identification of intermediate and final species in each one of the reaction steps
242 (see Table 3 and description of 'Thermogravimetric analysis and thermodynamic data for
243 destinezite' section) it is concluded that the final products, upon reaching the
244 temperature of 900°C, are rodolicoite, grattarolaite and hematite. This find justify the
245 selection of the previous temperature interval because the obtained final products have
246 been well identified and their enthalpy of formation ΔH_f^0 are known. Therefore, from the
247 thermodynamic data of these products and using the Hess's Law, it may be obtained the
248 enthalpy change ΔH of the balanced reaction representing the overall process for the
249 selected temperature range (50–900°C), and then it possible to determinate the enthalpy
250 of formation ΔH_f^0 of the destinezite. Applying a similar procedure, may be evaluated the
251 entropy change from DSC measurements, by dividing the corresponding enthalpy
252 change for each reaction step by the temperature. The standard entropy change (ΔS^0)
253 for the overall process, using again the Hess's Law may be computed (Anderson, 2005).
254 Therefore, it can be also estimated the standard entropy of formation ΔS_f^0 of the
255 destinezite by application of Hess' Law. Finally, these values were used to calculate the
256 standard Gibbs free energy of formation with $\Delta G_f^0 = \Delta H_f^0 - T\Delta S_f^0$, where ΔH_f^0 and ΔS_f^0

257 are, respectively, the standard enthalpy and entropy of formation determined from the
258 above calorimetric measurements, and T the standard temperature (298.15 K).

259 The values obtained of enthalpy, entropy, and Gibbs free energy of formation for the
260 destinezite have been compared with data estimated by non-experimental methods.
261 These crude estimates are mainly based on a) the ideal mixing model adopted by
262 [Nriagu and Dell \(1974\)](#), [Hemingway et al. \(2002\)](#) and [Gas'kova et al. \(2008\)](#), and b) the
263 theoretical approach adapted by [La Iglesia \(2009\)](#), based on the model of the
264 contribution of polyhedral units of [Hazen \(1985\)](#) and [Chermak and Rimstidt \(1989\)](#). The
265 latter method allows us to predict the values of $\Delta_f H^\circ$ and $\Delta_f G^\circ$ with an uncertainty of less
266 than 1.5% compared to those calculated from the experimental values. These estimates
267 show a good fit with the experimental results and led us to determine the solubility
268 product of other Fe-bearing phosphate minerals in order to discuss phase relationship
269 among minerals in the system Fe–P–S–O–H.

270 **Results**

271 **Mineralogical features of destinezite lumps**

272 Although the destinezite is invariably the main component (>95vol.%) of the lumps,
273 they usually enclose variable amounts of platy pseudo-hexagonal crystals of hematite of
274 several millimeters across, a few relics of partially oxidized subhedral magnetite and,
275 more rarely, small inclusions of monazite and quartz. In rare cases, the lumps retain
276 relics of a poorly characterized Fe phosphate mineral, whose variable composition
277 deviates from the ideal stoichiometry of common high-temperature anhydrous Fe
278 phosphate minerals (e.g., heterosite). Individual crystals of destinezite are not visible to

279 the naked eye, but are visible under the microscope. Texturally, they largely consist of
280 an aggregate of equigranular, interlocking, and randomly oriented anhedral to subhedral
281 grains (*de-1* in Fig. 3A). Locally, these aggregates seem to have recrystallized to
282 medium-grained polygonal aggregates, preferentially aligned along the wall of sealed
283 microfractures that crosscut the lumps. This second generation of destinezite (*de-2* in
284 Fig. 3A, 3B), with a platy shape and a pseudo-hexagonal outline (Fig. 3B, 4B), may attain
285 dimensions up to 50 μm across. The relative large size and the habit of the faceted
286 crystals of destinezite, in addition of their association with idiomorphic hematite (Fig.
287 4A), suggest that they grew as a result of the circulation of late hot solutions along the
288 fractures and pores in the lumps.

289 The determination of the optical properties of this destinezite is difficult, particularly
290 because of the small size of the crystals, their strong absorption, dispersion, and
291 anomalous extinction. Observed in thin section under transmitted plane-polarized light,
292 they show a continuous change in color, from yellow to deep brown to black, causing
293 irregular variations in birefringence, even at the scale of individual crystals. Rare
294 destinezite aggregates show an incipient replacement to a suite of secondary Fe
295 phosphate and sulfate minerals intermingled with supergene "limonite". These
296 secondary minerals may coat the aggregates, forming a layer up to 0.5 mm thick with a
297 rusty edge and an earthy brittle structure. They may also fill some crisscrossing
298 fractures, as thin films of submicroscopic aggregates exhibiting spherulitic micro-textures
299 (Fig. 3C). The X-ray diffraction and results of semi-quantitative EMP analyses of these
300 products indicate that they consist of variable proportions of diverse minerals, chiefly
301 cacoxenite, tenticite, rockbridgeite, and an uncommon Sr-rich jarosite (up to 5 wt% SrO)

302 (Fig. 3C).

303 The 'crystalline' hematite in the lumps presents similar characteristics to those of
304 the hematite that dominates in the sediments; the subhedral tabular to platy crystals
305 display a bright grey color. These grains are faceted (pinacoid, rhombohedron,
306 hexagonal prism), may exhibit skeletal textures, and locally attain several centimeters
307 across, which suggests growth under hydrothermal conditions ([Vorobyeva and Melnik,](#)
308 [1977](#); [Catling and Moore, 2003](#); [Demianets et al., 2003](#)). In some cases, the largest
309 grains host rare minute inclusions of chalcopyrite and euhedral pyrite, which indicates
310 that hematite and sulphides formed during the same hydrothermal event. In the more
311 oxidized samples, the edge of the hematite crystals is replaced by colloform goethite,
312 whereas the magnetite grains show evidences of supergene transformation to hematite.
313 However, this process did not reach completion, preserving abundant remnants of
314 magnetite within the secondary hematite.

315 **Chemical and isotopic composition of destinezite**

316 The average result of 40 selected EMP analyses (Table 2) reveals that the
317 composition of the destinezite is relatively uniform, in comparison with data reported in
318 the literature ([Matsubara et al., 1999](#); [Lledó, 2005](#)). With respect to the ideal formula, our
319 results indicate a slight excess of Fe and P and a deficiency in S. An indirect estimate of
320 the H₂O content by subtraction of the analytical total from 100% suggests ca. 5.5
321 molecules per cell. This figure is in accordance with the values estimated by [Matsubara](#)
322 [et al. \(1999\)](#), and previously reported by [Fleischer and Mandarino \(1995\)](#) and [Moiseeva](#)
323 [\(1967\)](#). However, these results disagree with the six molecules of H₂O in the ideal

324 formula proposed by [Peacor et al. \(1999\)](#), and the value obtained with the Penfield
325 method by [Anthony et al. \(2005\)](#) using samples of natural destinezite collected at Haut-
326 le-Bastia, Belgium. This apparent deficiency in H₂O could be presumably caused by the
327 damage or partial dehydration of the crystals under the EMP beam during the analysis,
328 even using defocused beams and short-duration counts. Although this explanation does
329 not satisfy the disagreement generated about the number of H₂O molecules in
330 destinezite, it indicates the ability to lose H₂O during the analyses in conditions close to
331 the ambient temperature (Fig. 4B). In fact, the color of this mineral easily changes when
332 it is observed in the field (reddish orange to brownish) compared to the laboratory
333 (yellowish orange), where it is in a dry atmosphere.

334 With respect to major elements, the results of the EMP analyses suggest a limited
335 substitution of SO₄ for PO₄, and minor or no substitution of Al for Fe³⁺ at the octahedral
336 sites of the structure. However, most of the analyses yield considerable amounts of SiO₂
337 (up to 4wt%; ca. 0.5 wt% on average), which probably reflects contamination by nano-
338 inclusions of quartz rather than substitution by SiO₄ at the tetrahedral sites. The
339 abundance of Ca in a large number of samples (up to 0.5 wt% CaO) could also reflect
340 contamination by admixtures of minerals resulting from the alteration of plagioclase in
341 the andesite, or the presence of traces of calcium-rich minerals (invisible nanoparticles
342 of anhydrite or gypsum?) derived from the destabilization of apatite. It is noteworthy that
343 apatite was not found in the nodules, nor in the horizons in which the destinezite occur.
344 However, it has been found in some pyroclastic or epiclastic horizons ([Nystrom and](#)
345 [Henríquez, 1994](#); [Nystrom et al., 2016](#)) far from areas affected by hydrothermal
346 alteration. As part of an ongoing investigation, values of $\delta^{34}\text{S}$ and $\delta^{18}\text{O}_{(\text{SO}_4)}$ values and

347 the Sr-isotope composition were determined for a few samples of pure destinezite, in
348 order to provide information on the source of S and the history of the fluids that have
349 participated in the formation of this mineral. Preliminary results have yielded $\delta^{34}\text{S}$ values
350 of 1.5 and 2.8 ‰ and $\delta^{18}\text{O}_{(\text{SO}_4)}$ values of 0.1 and 1.9 ‰ (two samples), and a range of
351 $^{87}\text{Sr}/^{86}\text{Sr}$ values between 0.7077 to 0.7081 (four samples; mean of 0.7080).

352 In addition to destinezite, we have also analyzed the rare remnants of Fe
353 phosphate grains found in the core of some lumps. Under the microscope, these relics
354 occur as nearly opaque inclusions less than 5–10 μm across. In thin section they show
355 a variable color, from deep reddish brown to dark green. They show irregular intricate
356 intergrowths with the host destinezite. Their distribution within the lumps is independent
357 of the open fractures that formed later. Analysis of these remnants indicates variable
358 and nonstoichiometric compositions, ranging from a SO_4 -free end-member with a
359 relatively high Fe_2O_3 content and anhydrous character to a SO_3 -rich and relatively
360 Fe_2O_3 -poor composition, close to the ideal stoichiometry of the destinezite. This
361 continuum clearly indicates that the majority of the compositions obtained indeed
362 represent admixtures of the two minerals. Most of our S-free results approach the
363 general formula $\text{Fe}^{2+}\text{Fe}^{3+}_2(\text{PO}_4)_2(\text{OH})_2$, which corresponds to lipscombite (see Table 2
364 for the average result of 14 selected analyses). This formula was obtained assuming
365 that the $\text{FeO}_{\text{total}}$ from the EMP analyses is recalculated to FeO and Fe_2O_3 according to
366 the ideal $\text{Fe}^{2+}/\text{Fe}^{3+}$ value of 1:2 proposed by [Yakubovich et al. \(2006\)](#) for minerals with
367 composition similar to the lipscombite–barbosalite family.

368 **Rietveld refinement of the destinezite structure**

369 [Peacor et al. \(1999\)](#) showed that destinezite from soils at Alum Cave Bluff, in
370 Tennessee, is triclinic. Its structure consists of infinite chains of $\text{Fe}-(\text{O},\text{OH},\text{H}_2\text{O})_6$
371 octahedra attached to sulfate and phosphate tetrahedra. These structural characteristics
372 should not change with minor variations in composition, which could include minor P-for-
373 S substitution, relatively high Fe contents, or a deficit in H_2O molecules as suggested by
374 our analyses. Neither should they vary with the apparent higher crystallinity shown by
375 our samples, as the grains show well-defined shapes and well-formed crystals (Fig. 3B,
376 4B). Accordingly, it seems appropriate to verify if the variations in grain size cited above
377 provide detectable modifications in the structure, especially considering that destinezite
378 used to solve the structure by [Peacor et al. \(1999\)](#) has a supergene origin.

379 The structure of the El Laco destinezite was refined using the FullProf code, in the
380 space group $P\bar{1}$ starting with the structure parameters refined by [Peacor et al. \(1999\)](#).
381 The bond lengths, bond angles and bond-valence summations are in good agreement
382 with the expected ones, which demonstrates conformity between the experimental and
383 calculated data. The final reliability factors are as follows: $R_p = 5.64$, $R_{wp} = 7.76$, Bragg
384 R-factor = 11.7, and $\text{Chi}^2 = 1.89$. As found by [Peacor et al. \(1999\)](#), our data indicate a
385 structure consisting of chains of octahedra containing Fe and O linked to sulfate and
386 phosphate tetrahedral forming layers parallel to (010). Interlayers of H_2O molecules
387 provide the hydrogen bonds that link the layers. The resulting structure resembles the
388 layers seen in clay minerals, which explains the platiness of the pseudo-hexagonal
389 crystals and cleavage observed under electron microscopy (Fig. 4B). The differences
390 between the cell parameter refined in our study [$a = 9.5828(2) \text{ \AA}$, $b = 9.7440(3) \text{ \AA}$, $c =$
391 $7.3302(3) \text{ \AA}$, $\alpha = 98.796(3)^\circ$, $\beta = 107.985(3)^\circ$, and $\gamma = 63.898(2)^\circ$] and the parameters

392 found by [Peacor et al. \(1999\)](#) and [Lledó \(2005\)](#) are very small or negligible, and within
393 the expected margins of the experimental error. These results confirm the relative
394 stability and tolerance of the crystal structure in spite of variations in composition,
395 degree of cohesion of the samples, and different environments of formation.

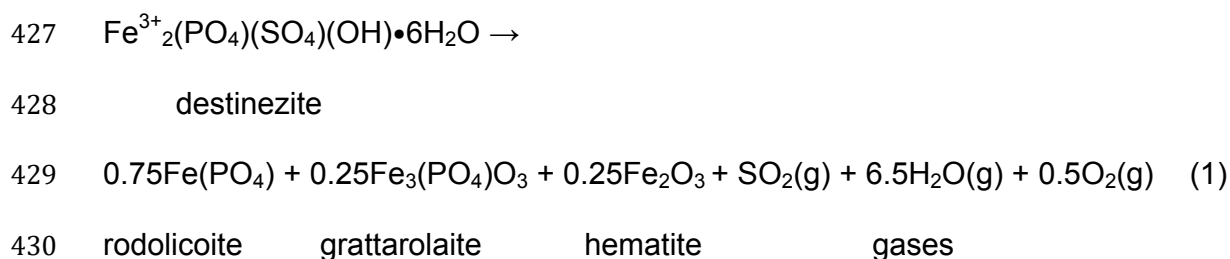
396 Although we do not have data to compare the degree of crystallinity between
397 subhedral destinezite and partially amorphous diadochite, our estimate of crystallite size,
398 ca. 250(50) nm, indicates that it is well above the limiting size typical of poorly crystalline
399 or partially amorphous materials. Usually, the size of particles in poorly crystalline
400 samples (i.e., crystalline polymers) is below 50 nm, and even less than 10–20 nm. The
401 average size of the crystalline domains (coherently diffracting domains) of the sample
402 can be estimated from the broadening of the signals using the Scherrer equation. From
403 the FullProf analysis, we also obtained the average apparent size of the crystals, ca.
404 230(5) nm, and the average maximum strain, ca. 0.17(3)%. These results are in good
405 accordance with the previously calculated crystalline size of the crystallites and confirm
406 the relatively coarse grain-size of the destinezite crystals.

407 **Thermogravimetric analysis and thermodynamic data for destinezite**

408 The results of TG/DTG experiments and the DSC calorimetric studies of the
409 destinezite (Fig. 5A, 5B) reveal several steps of mass loss with an increase of
410 temperature in the range between 50 and 900°C, which correspond to various
411 processes of decomposition. The DSC measurements shed light on the enthalpy change
412 (ΔH) associated with each of the thermogravimetric events encountered (Table 3). The
413 overall process could be described as follows: (i) The first two losses in weight upon

414 heating, observed at 50–110°C and 110–165°C, are attributed to the dehydration of the
415 mineral, whereas (ii) the third and fourth changes (at 165–350°C and 350–594°C,
416 respectively), could be related to the completion of dehydration and formation of an
417 intermediate complex consisting of lipscombite and an Fe-phosphate-rich product
418 (glass). The fifth step (iii) (594–648°C) could indicate the onset of dehydroxylation of the
419 lipscombite with the formation of mikasaite, followed by the progressive degradation by
420 thermal stress of the previously formed products. During this stage, one can expect the
421 formation of grattarolaite and the complete devolatilization of mikasaite. The last two
422 stages (iv) (at 648–725°C and 725–900°C, respectively) correspond to the complete
423 decomposition of lipscombite and mikasaite, concurrently with the final formation of
424 crystalline rodolicoite, grattarolaite, and hematite.

425 The overall thermal process of decomposition of destinezite may be summarized
426 by the following chemical equation:



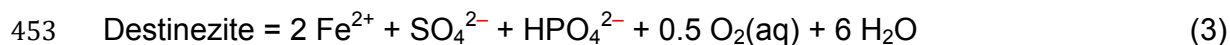
431 These reaction products are in good accordance with the results found by [Pieczara](#)
432 [et al. \(2017\)](#) in experiments using synthetic P-doped ferrihydrite and with the behavior of
433 the Fe–P–O system at high temperatures ([Wentrup, 1935](#); [Zhang et al., 2011](#)). The
434 same mineral assemblage was found at the Santa Barbara lignite mine, probably
435 derived from natural thermal alteration of vivianite in sediments ([Cipriani et al., 1997](#)).

436 Taking into account the reaction (1) and Hess's Law (2),

$$437 \quad \Delta H^{\circ} \text{rxn} = \sum \Delta H^{\circ}_f (\text{products}) - \sum \Delta H^{\circ}_f (\text{reactants}) \quad (2)$$

438 it is possible to calculate the standard enthalpy of formation of destinezite, taking into
439 account that $\Delta H^{\circ} \text{rxn}$ is the measured $\Delta H^{\circ} \text{DSC}$ at 900 °C (480 kJ/mol), and the
440 $\Delta H^{\circ}_f(\text{reactants})$ is equivalent to $\Delta H^{\circ}_f(\text{destinezite})$. From the enthalpy values
441 corresponding to $\Delta H^{\circ}_f(\text{products})$ that appear tabulated in the thermodynamic tables (i.e.
442 [Roine, 2002](#)), we have obtained the enthalpy value corresponding to destinezite: ($\Delta H^{\circ}_f =$
443 $-4051.7(4.3)$ kJ/mol) (Table 4). For the calculation of the standard entropy, we used the
444 same procedure as outlined in reaction (2), resulting in a value of $\Delta S^{\circ}_f(\text{destinezite}) = -$
445 $1518.5(20.0)$ kJ/mol (Table 4). Accordingly, applying the relationship $\Delta G^{\circ} = \Delta H^{\circ} - T\Delta S^{\circ}$,
446 we obtained a value of the Gibbs free energy of destinezite: $-3598.9(7.1)$ kJ/mol.

447 The above properties allow us to extend the default thermodynamic dataset LLNL
448 (compiled at the Lawrence Livermore National Laboratory) that makes use of the
449 Geochemist's Workbench (GWB) applications ([Bethke, 1996](#)) by adding destinezite to
450 the list of mineral phases. To calculate the solubility product, we have used the following
451 basic reaction of destinezite dissolution that involves only as basis the aqueous species
452 appropriate for the code:



454 From the standard-state free energies of formation of species in the reaction, the
455 calculated solubility product, expressed in logarithmic form, is $\log K(298) = -27.97(1.1)$.
456 According to [Anderson \(2005\)](#), both $\Delta H^{\circ} \text{r}$ and $\Delta S^{\circ} \text{r}$ are constants at the low
457 temperatures being considered (i.e., in the range typical of epithermal steam-heated

458 alteration, usually about 60–250°C). As a result, it is possible write, as an approximation,
459 $\Delta G^{\circ}(T) = \Delta H^{\circ}(298) - T\Delta S^{\circ}(298)$, where T is temperature in Kelvin. It is then possible
460 calculate the equilibrium constant for the above hydrothermal low-temperature range
461 with $\Delta G^{\circ}(T) = -RT\ln K$, using the data available from the literature for the species
462 mentioned in the dissolution reaction (3).

463 Discussion

464 The presence of anhydrous Fe phosphate minerals preserved as remnants in the
465 lumps, in addition of the size, morphology and location of these rocks, strongly support
466 the hypothesis that they track the existence of a Fe–P melt ejected by the volcano. Most
467 investigators of these rocks ([Haggerty, 1970a](#); [1976](#); [Lledó, 2005](#); [Mungall and Naslund,](#)
468 [2009](#); [Naslund et al., 2009](#); [Mungall et al., 2011, 2018](#)) have interpreted these minerals
469 as the product of the crystallization of a phosphate-rich melt that was immiscible in the
470 Fe-rich melt forming the El Laco magnetite deposit. Phosphate minerals like those
471 described here have been found as secondary phases in some granitic pegmatites
472 ([Baijot et al., 2014](#)) and meteorites ([Buseck and Holdsworth, 1977](#)), suggesting a
473 magmatic affiliation.

474 At El Laco, textures considered indicative of phosphate minerals crystallized from a
475 melt, such as the presence of meniscus, rounded aggregates and spherical inclusions,
476 were probably destroyed during their replacement by destinezite. However, [Mungall et](#)
477 [al. \(2018\)](#) have described evidences of the existence of such a liquid in the hematite-rich
478 sediments, in the form of complex fine-grained Fe phosphate minerals enclosed within
479 euhedral hematite crystals or armored by hematite aggregates. An Fe phosphate phase

480 similar to that found in the core of the destinezite lumps has also been found in material
481 cementing ash-sized hematite. Its composition approaches an unidentified anhydrous Fe
482 phosphate of formula $\text{Fe}^{2+}_3\text{Fe}^{3+}(\text{PO}_4)_3$ and is possibly related to vivianite, phosphoferrite,
483 or lipscombite according to the description of [Haggerty \(1970b,1991\)](#). Analyses of the
484 same material provided by [Mungall and Naslund \(2009\)](#) and [Mungall et al., \(2018\)](#) also
485 indicate the presence of similar minerals with the general formula $\text{Fe}_5(\text{PO}_4)_4(\text{OH})_3 \cdot 2\text{H}_2\text{O}$,
486 which are comparable to beraunite, dufrénite, or ferrian giniite. In addition to these
487 variable results in the composition of the interstitial phosphates, [Lledó \(2005\)](#) reported
488 on diadochite from El Laco, with an unusually high Fe content, up to 58.4 wt.% Fe_2O_3 .
489 As a whole, these analytical results point to a mixture of minerals, with prevalence of
490 lipscombite over destinezite. We believe that lipscombite probably is the main product of
491 the hydrothermal recrystallization of an unknown high-temperature phosphate precursor
492 that solidified from a residual melt near the Fe_2O_3 – FePO_4 eutectic ([Mungall et al., 2018](#)).
493 Thus we assume that the lipscombite, found as a relict secondary mineral, formed at the
494 expense of a magmatic mineral.

495 **The hydrothermal formation of destinezite**

496 The intergrowth of the destinezite with gray hematite, as well as the presence of
497 relics of lipscombite, which is devoid of S, the relative large grain-size of the destinezite
498 crystals, and the presence of jarosite replacing the edge of the grains, all suggest that
499 the destinezite formed by reaction of a phosphate precursor with late fluids. Reaction of
500 a SO_2 -rich gas exsolved during the crystallization of the Fe-rich melts with vadose water
501 ([Sillitoe and Burrows, 2002](#); [Tornos et al., 2017](#)) could have promoted the transformation
502 of lipscombite and related phases to destinezite. The inferred hydrothermal

503 decomposition requires a chemical environment with variable activities of phosphate and
504 sulfate, at temperatures below 300°C, and high fluid pressures. These conditions
505 typically occur in low-sulfide oxidized systems ($\text{SO}_4^{2-} \rightarrow \text{H}_2\text{S}$) characterized by an
506 abundance of sulfate of steam-heated origin, as proposed by [Sillitoe and Burrows](#)
507 [\(2002\)](#). The presence of lipscombite and the described scenario preclude other
508 mechanisms for the formation of destinezite, such as its direct precipitation from fluids
509 generated from the remobilization of the apatite–magnetite ores. In this scenario, a large
510 part of the magnetite was replaced by maghemite as a metastable intermediate
511 transformation phase, and ultimately to hematite as the end product (up to 40%
512 according to [Tornos et al. 2017](#)), with most of the apatite being completely destroyed.

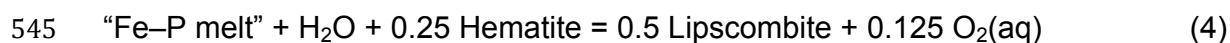
513 Our preferred model for the formation of destinezite involves a complex
514 polyphase evolution with two distinct steps: (i) an early stage of crystallization of a
515 hypothetical Fe phosphate precursor, followed by (ii) a second stage of intense
516 sulfidation of the former phosphate mineral and oxidation of the magnetite. Finally, both
517 processes were followed by an incipient stage of supergene alteration observed only at
518 the edges of some broken lumps.

519 ***1 Early stage***

520 The conditions of formation of the hypothetical phosphate precursors are difficult
521 to estimate. However, the formation of lipscombite has been obtained under
522 hydrothermal conditions by transformation of ferric phosphate phases over the
523 temperature range between 110°C and 560°C ([Gheith, 1953](#); [Song et al., 2005](#);
524 [Yakubovich et al., 2006](#)). These experiments have yielded hydroxylated Fe phosphate

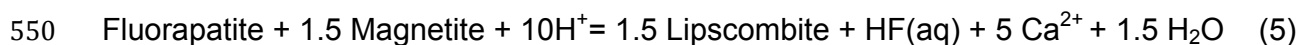
525 compounds of variable composition whose stability and structural organization are
526 determined by the ratio of Fe²⁺ to Fe³⁺, which depends on the oxygen fugacity of the
527 system; in the case of lipscombite, that ratio is 1:2 according to [Yakubovich et al.,](#)
528 [\(2006\)](#). According to [Gheith \(1953\)](#), lipscombite containing a high proportion of trivalent
529 Fe can form from heterosite or rodolicoite in the presence of Fe oxide below 560°C, if
530 the ferric ions are partially reduced. This temperature limit agrees with our calorimetric
531 experiments, in which the lipscombite remains stable up to its final destabilization
532 (dehydroxylation) at about ca. 600°C. Lipscombite is more likely to form at high to
533 moderate temperatures by hydrothermal processes in volcanic environments
534 characterized by high values of oxygen fugacity. Also, the redox conditions suggested
535 seem to be consistent with those at El Laco, which is characterized by an unusually high
536 fO₂ that allows anhydrite to be stable from magmatic to hydrothermal conditions ([Tornos](#)
537 [et al., 2017](#)). In any case, and despite the complex thermal behaviour of this mineral in
538 an oxygenated environment ([Song et al., 2005](#)), the above studies support a magmatic-
539 hydrothermal derivation for the iron phosphate precursor preserved in the core of some
540 lumps.

541 Replacement of the presumed primary (magmatic?) phosphate minerals by
542 lipscombite requires high P and low sulfate contents in the system. The precipitation of
543 lipscombite most likely arises by a chemical reaction involving an aqueous phosphate
544 derived from the consolidated Fe–P melt and hematite from the tephra:

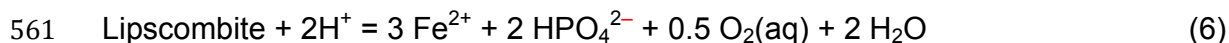


546 In the formulation of this reaction, we have taken rodolicoite as a proxy for the solidified

547 Fe–P-rich melt. The alteration of the pristine magmatic phosphate (i.e., fluorapatite)
548 present in the host rocks and ores could proceed in the presence of magnetite under
549 acidic conditions:



551 At an early hydrothermal stage of alteration, large amounts of phosphate could be
552 released to the fluids, facilitating the replacement of the precursor Fe phosphate
553 minerals. If this hypothesis holds, the lipscombite remnants in the lumps would have
554 formed early, likely at conditions of high or moderate temperature. We do not know the
555 requirement under which these reactions take place, but it is possible to discuss the
556 conditions of thermodynamic stability of these minerals in light of the estimate of the
557 Gibbs free energy of formation using the predictive method proposed by [Nriagu \(1976\)](#)
558 and data from [Nriagu and Dell \(1974\)](#). The dissociation constant for lipscombite, \log
559 $K(298) = -22.87$, was calculated from the following dissolution reaction through the
560 GWB program ([Bethke, 1996](#)):

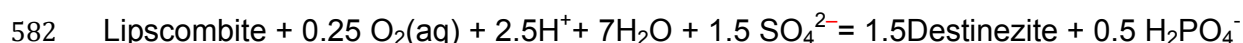


562 According to the activity–activity diagrams (Fig. 6), lipscombite is prevalent at
563 relatively high temperatures, where high concentrations of phosphate are present in the
564 fluid. To favor the stabilization of lipscombite, we have assumed geologically reasonable
565 hydrothermal conditions, with a temperature of ~300–200°C, a moderately acidic fluid,
566 and realistic activities of Ca^{2+} and K^+ (10^{-2}), keeping low the activity of SO_4^{2-} .
567 Interestingly, the diagrams in Figure 6 reveal a significant reduction in the stability field
568 of lipscombite if temperature or pH decreases. Significantly, the above conditions

569 preclude the occurrence of jarosite and destinezite. The diagrams also show that the
570 apatite saturation-line is clearly pH-dependent (Fig. 6A). The formation of fluorite is
571 favored by the destabilization of fluorapatite if the concentration of F reaches high levels
572 at the assumed conditions, which probably explain the occurrence of fluorite crystals
573 coating euhedral magnetite in some ore bodies ([Tornos et al., 2017](#)).

574 **2 Sulfidation stage**

575 The replacement of lipscombite by destinezite involves a dramatic increase of the
576 activity of sulfate (Fig. 6B) and a strong decrease in the activity of P. Conditions inferred
577 for this reaction entail a highly oxidizing and acidic (pH < 3) environment that is
578 compatible with the formation of steam-heated systems, as a result of condensation of
579 magmatic vapor in groundwater at temperatures that seldom exceed 200°C ([Sillitoe,](#)
580 [1993](#); [Hedenquist and Taran, 2013](#); [Sillitoe, 2015](#)). Under these circumstances,
581 lipscombite can almost be destabilized to destinezite:



583 (R-7)

584 A comparison of the stability fields of the minerals involved indicates that at
585 temperatures below ca. 150°C, lipscombite is no longer stable (Fig. 6C), whereas the
586 stability field of the destinezite + hematite assemblage is favored (hatched areas in Fig.
587 6).

588 The $\delta^{34}\text{S}$ values of two samples of destinezite ($\delta^{34}\text{S}_{\text{SO}_4} = 1.5, 2.8\text{‰}$) are
589 significantly lower than the magmatic-hydrothermal signature of sulfate minerals that
590 typically record sulfate coexisting with reduced S derived from the disproportionation of

591 magmatic SO₂, between 20 and 25‰, according to [Rye \(2005\)](#). The above values
592 suggest that the system likely was strongly oxidized, and that all the S was in the form of
593 sulfate. The precipitate, destinezite, inherited the original signature of the melt, as can
594 be expected in a steam-heated system ([Rye, 2005](#)). These values are consistent with
595 the reaction of lipscombite with fluids within a steam-heated system. The oxygen isotope
596 data of the same samples of destinezite plot away from those of magmatic fluids. They
597 are close to 0‰ ($\delta^{18}\text{O}_{(\text{SO}_4)}$ values of 0.1 and 1.9‰), indicating that the oxygen was not of
598 magmatic origin but dominantly meteoric ([Rye, 2005](#)), perhaps with a minor contribution
599 from an ¹⁸O-enriched source that could either be the magmatic gas or the replaced
600 andesite at a high fluid:rock ratio. Preliminary Sr isotope data for four samples
601 ($^{87}\text{Sr}/^{86}\text{Sr}_{\text{avg}} = 0.7080$) reveal values that are higher than most of the reported values for
602 the El Laco andesite (between 0.7066 and 0.7074 according to [Tornos et al., \(2017\)](#), but
603 are lower than the values of the magnetite–apatite rocks ($^{87}\text{Sr}/^{86}\text{Sr} \approx 0.7083$; [Tornos et
604 al., 2017](#)). These values are also consistent with a mixture of Sr inherited from the
605 magmatic fluids and the host andesite rocks. Alternatively, the Sr could be derived from
606 andesite equilibrated with fluids exsolved from the Fe-rich melt. In brief, the isotopic data
607 suggest that the S and oxygen of the destinezite are inherited from the superimposed
608 steam-heated alteration.

609 Interestingly, we have not detected Al phosphate–sulfate minerals (APS, i.e.,
610 woodhouseite, crandallite, svanbergite) in the lumps. These minerals can coexist with
611 alunite or kaolinite in zones of advanced argillic alteration ([Stoffregen and Alpers, 1987](#)).
612 The lack of APS minerals in steam-heated alteration zones at El Laco is interpreted as
613 being indicative of a shortage of P in later fluids or, alternatively, a paucity of primary

614 apatite in the host rocks. Thus, the lack of these minerals in altered areas from El Laco
615 proves that the activity of phosphate during most of the stages of the steam-heated
616 alteration process was low; the major source of P in forming destinezite was the
617 immiscible phosphate melts ejected by the volcano.

618 Contrary to a previous report concerning the APS, variscite has been found in
619 zones at El Laco in that have undergone intense steam-heated alteration (e.g., Cristales
620 Grandes, Fig.1). According to our model, variscite extends its stability field into the
621 region of low and moderate pH, even at very low phosphate concentrations (Fig. 6D).
622 Interestingly, this diagram shows that the variscite–alunite boundary roughly overlies the
623 position of the destinezite–hematite boundary. Thus, mineral assemblages with variscite
624 and alunite or hematite or both ([Dill, 2001](#)) are compatible with the formation of
625 destinezite during the waning stage of steam-heated alteration. Variscite probably
626 formed coevally with destinezite and alunite at a stage when the dissolved Al, mainly
627 from the breakdown of plagioclase, was incorporated into the fluids. The virtual absence
628 of pyrite and the ubiquitous presence of alunite and gypsum everywhere are in good
629 agreement with the proposed scenario.

630 ***3 Final supergene stage***

631 The rare replacement of destinezite by Sr-rich jarosite indicates that the surface
632 runoff waters at El Laco had a rather abundant concentration of K, Sr, and sulfate,
633 sufficient to promote the supergene replacement of destinezite by jarosite. Similarly,
634 some lumps exposed to acidic meteoric solutions show an alteration along rims
635 consisting of a mixture of cacoxenite, tinticite, and strengite mixed with earthy goethite.

636 In these surficial environments, the field of stability of tenticite coincides with that of
637 cacoxenite, both being stable under oxidizing and acidic conditions ([Nriagu and Dell,
638 1974](#)). All these products derived from the alteration of destinezite, are unequivocally of
639 supergene origin, and prove the early and hypogene character of this mineral.

640 **Implications**

641 Our research demonstrates that the rare lumps of destinezite (e.g., Fe–P–S-rich
642 tephra) found in the hematite-rich sediments that infill crater lakes at El Laco volcano are
643 the result of a complex evolution of an immiscible phosphate-rich melts erupted by the
644 volcano. This transformation of the pyroclasts to destinezite happened during the
645 hydrothermal alteration of the volcanic rocks to alunite, mainly provoked by the cooling
646 and the active circulation of oxidizing waters after eruption. During this process, the Fe–
647 P-rich immiscible fraction of the melt separated from the parent silicate magma and was
648 almost entirely destabilized to lipscombite and later, to destinezite. Concurrently, a large
649 part of the magnetite ores and Fe oxide ashes underwent oxidation.

650 This finding can provide key constraints on the long-standing controversy about
651 whether the Fe oxide–apatite deposits are magmatic or hydrothermal in origin. Until this
652 point, most studies on the origin of the magnetite–apatite deposits as a result of
653 magmatic immiscibility have been confined to the study and interpretation of melt
654 inclusions hosted within pyroxene and plagioclase phenocrysts, the geochemistry of the
655 volcanic rocks, and interpretations of magma sources on the basis of isotopic indicators.
656 However, the occurrence of Fe–P-rich pyroclasts transformed to destinezite provides a
657 striking direct confirmation that such magmas exist and should be considered an

658 additional source of information.

659 The hydrothermal transformation of the above Fe–P-rich melt to almost
660 monomineralic destinezite took place in a steam-heated environment fed by deeper
661 boiling fluids near the surface (acid sulfate waters). This hypogenic interpretation for the
662 El Laco destinezite has two major implications: (1) this mineral represents the final
663 product of the replacement of a pristine immiscible Fe–P-rich melt ejected by the
664 volcano, and (2) destinezite may form over a range of geological environments that is
665 much broader than is currently assumed. It has heretofore invariably been viewed as
666 having a supergene derivation.

667 In order to fill the gap of thermodynamic data necessary to discuss the stability
668 domains of assemblages of hydrated Fe phosphate–sulfate and Fe oxide minerals, and
669 to be able to predict the conditions favorable for the formation of destinezite, we
670 measured the thermal decomposition of this mineral by the classical TGA and DSC
671 techniques. With those results, we have derived its enthalpy, entropy, free energy of
672 formation, and the equilibrium constant for its dissolution reaction. These new
673 thermodynamic values have been used to calculate mineral-stability diagrams in
674 activity–activity coordinates. These are then used to identify environmental conditions
675 under which the destinezite + hematite association is thermodynamically stable. From
676 these thermodynamic properties, it follows that the destinezite behaves as a stable
677 mineral over a wide range of hydrothermal conditions, provided that the hydrothermal
678 environment is acidic, the temperature is low (<150°C), and the sulfate contents are high
679 to very high, keeping the P concentrations low in the fluids. These thermodynamic
680 constraints agree well with the physicochemical characteristics of the El Laco

681 hydrothermal area, which has been subjected to pervasive steam-heated alteration.

682

683 **Acknowledgments**

684 The authors are grateful to Robert Martin, and an anonymous reviewer, for critical
685 reading, constructive comments, and help in improving the clarity of our manuscript. We
686 thank Alfonso Pesquera for critical discussion of a first version of this manuscript. We
687 are also grateful to Javier Sangüesa and Gabriel A. López for their assistance with the
688 XRD and SEM-EDS analyses, respectively. This study was financially supported by the
689 Department of Education, Universities and Research of the Basque Government (IT762-
690 13, and IT-779–13), and the Spanish Government (Ministerio de Economía y
691 Competitividad), FEDER funds MAT2015-6641-P and CGL2011-23207. We appreciate
692 also the Compañía Minera del Pacífico for assistance and granting access to the mine.

693

694 **References**

- 695 Anderson, G. (2005) Thermodynamics of Natural Systems. Cambridge University Press, 648.
- 696 Anthony, J., Bideaux, R., Bladh, K., and Nichols, M.E. (2005) Diadochite. (Eds.), Handbook of Mineralogy,
697 Mineral Data Publishing, version 1, V,
698 <http://www.handbookofmineralogy.org/pdfs/diadochite.pdf>.
- 699 Baijot, M., Hatert, F., and Dalbo, F. (2014) Mineralogy and Petrography of phosphate mineral
700 associations from the Joçcao pegmatite, Minas Gerais, Brazil. The Canadian Mineralogist, 52,
701 373-397.
- 702 Bethke, C. (1996) Geochemical Reaction Model. Oxford University Press, New York oxford, 397.

- 703 Broughm, S.G.B., Hanchar, J.M., Tornos, F., Westhues, A., and Attersley, S. (2017) Mineral chemistry of
704 magnetite from magnetite-apatite mineralization and their host rocks: examples from Kiruna,
705 Sweden, and El Laco, Chile. *Mineralium Deposita*, 52(8), 1223-1244.
- 706 Buseck, P., and Holdsworth, E. (1977) Phosphate minerals in pallasite meteorites. *Mineralogical*
707 *Magazine*, 41, 91-102.
- 708 Catling, D., and Moore, J. (2003) The nature of coarse-grained crystalline hematite and its implications
709 for the early environment of Mars. *Icarus*, 165, 277-300.
- 710 Cipriani, C., Mellini, M., Pratesi, G., and Viti, C. (1997) Rodolicoite and grattarolaite, two new phosphate
711 minerals from Santa Barbara Mine, Italy. *European Journal of Mineralogy*, 9, 1101-1106.
- 712 Chermak, J., and Rimstidt, J. (1989) Estimating the thermodynamic properties (AGP and All8) of silicate
713 minerals at 298 K from the sum of polyhedral contributions. *American Mineralogist*.
- 714 Dare, S.A.S., Barnes, S., and Beaudoin, G. (2015) Did the massive magnetite "lava flows" of El Laco (Chile)
715 form by magmatic or hydrothermal processes? New constraints from magnetite composition by
716 LA-ICP-MS. *Mineralium Deposita*, 50, 607-617.
- 717 Demianets, L., Pouchko, S., and Gaynutdinov, R. (2003) Fe₂O₃ single crystals: hydrothermal growth,
718 crystal chemistry and growth morphology. *Journal of Crystal Growth*, 259, 165-178.
- 719 Dill, H. (2001) The geology of aluminium phosphates and sulphates of the alunite group minerals: A
720 review. *Earth Science Reviews*, 53, 35-93.
- 721 Fleischer, M. F., and Mandarino, J.A. (1995) Glossary of mineral species 1995. *The Mineralogical Record*.
722 Tucson, vi +280pp ISBN 1062 3531.
- 723 Gas'kova, O.L., Shironosova, G.P., and B., B.S. (2008) Thermodynamic estimation of the stability field of
724 bukovskyite, an iron sulfoarsenate *Geochemistry International*, 46(1), 85-91.
- 725 Gheith, M. (1953) Lipscombite: A new synthetic "Iron lazulite". *American Mineralogist*, 38, 612-628.
- 726 Haggerty, S. (1970a) The Laco magnetite lava flow, Chile. *Carnegie Institution of Washington*, 68, 329-
727 330.
- 728 Haggerty, S. (1970b) A new iron-phosphate mineral. *Carnegie Institution of Washington*, 68, 330-332.
- 729 Haggerty, S. (1976) Opaque mineral oxides in terrestrial igneous rocks. In: Rumble, D. (ed.), III, *Oxide*
730 *Minerals. Miner. Soc. Am. (Short Course Notes)*, 3, Chapter 8, 101-300.
- 731 Haggerty, S. (1991) Chapter 5. Oxide Textures. A Mini-Atlas. in: Lindsley, D.H. (ed) *Oxide Minerals:*
732 *Petrologic and magnetic significance. Reviews in Mineralogy*, 25, 129-219.

- 733 Hazen, A. (1985) Comparative crystal chemistry and the polyhedral approach. In: Microscopic to
734 macroscopic: Atomic environment to mineral thermodynamic. in: Kieffer, S.W. and Navrotsky, A.
735 (eds.), Mineralogical Society of America. Reviews in Mineralogy, 14, 317-345.
- 736 Hedenquist, J.W., and Taran, Y. (2013) Modeling the formation of advanced argillic lithocaps: Volcanic
737 vapor condensation above porphyry intrusions. *Economic Geology*, 108(7), 1523-1540.
- 738 Hemingway, B.S., Seal, R.R., and Chou, I.M. (2002) Thermodynamic data for modeling acid mine drainage
739 problems: Compilation and estimation of data for selected soluble iron-sulfate minerals. Open-
740 File Report, 02-161 1-13.
- 741 Henriquez, F., and Martin, R.F. (1978) Crystal-growth textures in magnetite flows and feeder dykes, El
742 Laco, Chile. *The Canadian Mineralogist*, 16, 581-589.
- 743 Henriquez, F., Naslund, H.R., Nystrom, J., Vivallo, W., Aguirre, R., Dobbs, F., and Lledó, H. (2003) New
744 field evidence bearing on the origin of the El Laco magnetite deposit, Northern Chile - A
745 discussion. *Economic Geology*, 98, 1497-1502.
- 746 Henríquez, F., and Nyström, J. (1998) Magnetite bombs at El Laco volcano, Chile. *GFF*, 120, 269-271.
- 747 Keller, T., Hanchar, J.M., Tornos, F., and Suckale, J. (2018) Formation of the El Laco magmatic magnetite
748 deposits by Fe-Si melt immiscibility and bubbly suspension flow along volcano tectonic faults. Fall
749 Abstract. Meeting American Geophysical Union, Washington.
- 750 La Iglesia, A. (2009) Estimating the thermodynamic properties of phosphate minerals at high and low
751 temperature from the sum of constituent units. *Estudios Geológicos*, 65(2), 109-119.
- 752 Lledó, H. (2005) Experimental studies on the origin of iron deposits and mineralization of Sierra La
753 Bandera, Chile. Ph D thesis Binghamton University, State University of New York, p. 271.
- 754 Matsubara, S., Miyawaki, R., and Iwano, S. (1999) Diadochite from the Hinomaru-Nako Mine, Yamaguchi
755 Prefecture, Japan. *Bulletin National Science Museum, Tokyo, Japan*, 25(1-2), 51-57.
- 756 Moiseeva, M. (1967) O nakhodke destinezita v Kuraminskom Khrebte. . *Dokl Akad Nauk Uzb SSR Chem*
757 *Abstract* 9, 45-47.
- 758 Moiseeva, M. (1970) Mineralogiya kori vivetrivaniya Kura-minskogo khrebta i usloviya e obrazovaniya.
759 *Zap. Uzb. Otd. Vses Mineral O-va*, Chem. Abstract 75: 23, 46-54.
- 760 Mungall, J., Long, K., Brenan, J., Smythe, D., and Naslund, H. (2018) Immiscible shoshonitic and Fe-P-
761 oxide melts preserved in unconsolidated tephra at El Laco volcano, Chile. *Geology*, 46(3), 255-
762 258.
- 763 Mungall, J., and Naslund, H.R. (2009) Melt inclusions in Fe oxide and phosphate tephra of El Laco
764 volcano, Chile. AGU Abstract, Code 2009AGUSM.V12A, 04M.

- 765 Mungall, J.E., Long, K., Brenan, J., and Naslund, R. (2011) Formation of iron oxide and phosphate tephra
766 of the El Lago Volcano, Chile from an Fe-P-O-S magma. Dissertation
767 (<http://www.tgdg.net/Resources/Documents/Mungall%20El%20Laco%20Brazil%202011.pdf>).
- 768 Naranjo, J., Henriquez, F., and Nystrom, J. (2010) Subvolcanic contact metasomatism at El Lago Volcanic
769 Complex, Central Andes. *Andean Geology*, 37, 110-120.
- 770 Naslund, H.R., Henriquez, F., Nystrom, J., Aguirre, R., and Lledó, H. (2003) El Lago, Chile: Evidence for
771 eruption of an immiscible Fe-O-S-P melt. Seattle Annual Meeting of the Geological Society of
772 America. Paper N° 149-4.
- 773 Naslund, H.R., Henriquez, F., Nystrom, J., Vivallo, W., and Dobbs, F. (2002) Magmatic iron ores and
774 associated mineralizations: Examples from the Chilean High Andes and Coastal Cordillera. In:
775 Porter T.M., (ed), *Hydrothermal Iron Oxide Copper-Gold & Related. Deposits: A Global*
776 *Perspective*, 2(PGC Publishing, Adelaide), 207-226.
- 777 Naslund, H.R., Mungall, J., Henriquez, F., Nystrom, J., Lledó, H., Lester, G., and Aguirre, R. (2009) Melt
778 inclusions in silicate lavas and iron-oxide tephra of the El Lago volcano, Chile. XII Congreso
779 Geológico Chileno, Santiago, 22-26 Noviembre, 1-4.
- 780 Nickel, E., and Nichols, M. (1991) *Mineral Reference Manual*. Springer Science+Busines Media New York,
781 ISBN 978-1-4613-6634-8, 378 pp.
- 782 Nriagu, J., and Dell, C. (1974) Diagenetic formation of iron phosphates in recent lake sediments.
783 *American Mineralogist*, 59, 934-946.
- 784 Nriagu, J.O. (1976) Phosphate - clay mineral relations in soils and sediments. *Canadian Journal of Earth*
785 *Sciences*, 13(6), 717-736.
- 786 Nystrom, J., and Henríquez, F. (1994) Magmatic features of iron ores of the Kiruna type in Chile and
787 Sweden: ore textures and magnetite geochemistry. *Economic Geology*, 89, 820-839.
- 788 Nystrom, J., Henríquez, F., Naranjo, J., and Naslund, H.R. (2016) Magnetite spherules in pyroclastic iron
789 ore at El Lago, Chile. *American Mineralogist*, 101, 587-595.
- 790 Ovalle, J., La Cruz, N., Reich, M., Barra, F., Simon, A.C., Konecke, B., Rodriguez-Mustafa, M., Deditius, A.,
791 Childress, T., and Morata, D. (2018) Formation of massive iron deposits linked to explosive
792 volcanic eruptions. *Scientific Reports*, 8, 1-11.
- 793 Peacor, D., Roland, R., Coskren, T., and Essene, E. (1999) Destinezite-("diadochite"),
794 Fe₂(PO₄)(SO₄)(OH).6(H₂O): its crystal structure and role as a soil mineral at Alum Cave Bluff,
795 Tennessee. *Clay and Clay Minerals*, 47, 1-11.

- 796 Pieczara, G., Borkiewicz, O., and Manecki, M. (2017) Rodolicoite and grattarolaite, intermediates in the
797 thermal transformation of synthetic P-doped ferrihydrite. *Geophysical Research Abstracts*, 19,
798 EGU2017-9305.
- 799 Pouchou, J.L., and Pichoir, J. (1984) A new model for quantitative x-ray microanalysis. Part I: application
800 to the analysis of homogeneous samples. *RechercheAerospatial*, 3, 167-192.
- 801 Rhodes, A., Oreskes, N., and Sheets, S. (1999) Geology and rare earth element geochemistry of
802 magnetite deposite at El Laco, Chile. In: Skinner, B.J.,(ed), *Geology and ore deposits of the Central*
803 *Andes*, Society of Economic Geologists, Special Publication, 7, 299-332.
- 804 Rodríguez-Carvajal, J. (2001) Recent Developments of the Program FULLPROF, in Commission on Powder
805 Diffraction (IUCr). *Newsletter* 26, 12-19.
- 806 Rye, R. (2005) A review of the stable-isotope geochemistry of sulfate minerals in selected igneous
807 environments and related hydrothermal systems. *Chemical Geology*, 215, 5-36.
- 808 Sillitoe, R.H (1993) Epithermal models: Genetic types, geometrical controls, and shallow features: .
809 Geological Association of Canada Special Paper 40, 403-417.
- 810 Sillitoe, R.H. (2015) Epithermal paleosurfaces. *Mineralium Deposita*, 50, 767-793.
- 811 Sillitoe, R.H, and Burrows, D. (2002) New field evidence bearing of the origin of the El Laco magnetite
812 deposit, northern Chile. *Economic Geology*, 97, 1101-1109.
- 813 Song, Y., Zavalij, P., Chernova, N., and Wittingham, M. (2005) Synthesis, crystal structure, and
814 electrochemical and magnetic study of new iron (III) hydroxyl-phosphates, isostructural with
815 lipscombite. *Chemistry of Materials*, 17, 1139-1147.
- 816 Stoffregen, R., and Alpers, C. (1987) Woodhouseite and svanbergite in hydrothermal ore deposits:
817 Products of apatite destruction during advanced argillic alteration. *The Canadian Mineralogist*,
818 25, 201-211.
- 819 Tornos, F., Velasco, F., and Hanchar, J. (2016) Iron oxide melts, magmatic magnetite, and superheated
820 magmatic-hydrothermal systems: The El Laco Deposit, Chile. *Geology*, 44 427-430.
- 821 Tornos, F., Velasco, F., and Hanchar, J. (2017) The magmatic to magmatic-hydrothermal evolution of the
822 El Laco Deposit (Chile) and its implications for the genesis of magnetite-apatite deposits.
823 *Economic Geology*, 112, 1595-1628.
- 824 Tornos, F., Hanchar, J.M., Velasco, F., Muñizaga, R., and Levresse, G. (2017) The roots and tops of
825 magnetite-apatite mineralization: Evolving magmatic-hydrothermal systems. 14th SGA Biennial
826 Meeting, Quebec City.

- 827 Velasco, F., and Tornos, F. (2012) Insights on the effects of the hydrothermal alteration in the El Laco
828 magnetite deposit (Chile). *Macla*, 16, 210-211.
- 829 Velasco, F., Tornos, F., and Hanchar, J. (2016) Immiscible iron- and silica-rich melts and magnetite
830 geochemistry at the El Laco volcano (northern Chile): Evidence for a magmatic origin for the
831 magnetite deposits. *Ore Geology Reviews*, 79, 346-366.
- 832 Vorobyeva, K.A., and Melnik, Y.P. (1977) An experimental study of the system of Fe₂O₃-H₂O at T =100-
833 200 °C and P up to 9 kilobars. *Geochemistry International*, 8, 108-115.
- 834 Wentrup, H. (1935) Contribution on the system iron-phosphorus-oxygen. *Archiv fur Eisenhüttemwesen*,
835 9(7), 57-60.
- 836 Yakubovich, O., Steele, I., Rusakov, V., and Urusov, V. (2006) Hole Defects in the Crystal Structure of
837 Synthetic Lipscombite (Fe_{4.7}Fe_{2.3})[PO₄]₄O_{2.7}(OH)_{1.3} and Genetic Crystal Chemistry of
838 Minerals of the Lipscombite-Barbosalite Series. *Crystallography Reports*, 51(3), 401-411.
- 839 Zhang, L., Schlesinger, M., and Brow, R. (2011) Phase Equilibria in the Fe₂O₃-P₂O₅ System. *Journal of American Ceram*
840 *Soc*, 94(5), 1605-1610.

841

842

843

844

845

846 **Figure captions and Tables**

847 Figure 1 Schematic geological map of the El Laco volcano, northern Chile (A) showing
848 the major magnetite-apatite deposits (black areas) and zones of hydrothermal alteration
849 (red areas) hosted in the Pliocene andesitic rocks (modified from [Tornos et al., 2016](#)).
850 Star symbol indicates the main location of the destinezite-rich rocks near the Laco Sur
851 ore body. (B) General view of El Laco volcano from south. Note the zone of intense

852 alunitization of the volcanics at the south slope of the mountain (light colour is the Pasos
853 Blancos area).

854 Figure 2 (A) Unconsolidated hematite-rich epiclastic deposits beneath the Laco Sur
855 orebody showing a crude layering and poor grain sorting. The horizon containing
856 destinezite lumps displays intense orange color. (B) Cluster of destinezite fragments
857 with size between 2 and 10 cm in diameter belonging to the same chaotic layer. The
858 layer is mainly composed of rubble and fine-grained debris of hematite and is interpreted
859 as representing surge deposits deposited into a crater lake. Note the intense
860 fragmentation and the angled character of the destinezite clasts.

861 Figure 3 Photomicrographs of El Laco destinezite. (A) Massive fine-grained destinezite
862 (de-1) criss-crossed by multiple fractures rimmed by coarse grained destinezite (de-2);
863 hematite crystals (hm) usually occur near these microfractures. (B) Large coarse-
864 grained subhedral destinezite crystals (de-2) overgrowing primary massive aggregates
865 close to the microveins; lighter edges and dark core sectors (brown colors) in some
866 crystals indicate incipient transformation to supergene iron-phosphate products
867 (tinticite?). (C) Porous incrustations of supergene Sr-rich jarosite (Sr-jar) associated with
868 spherulitic cacoxenite (radiate fibrous growth) that occasionally occur coating some
869 destinezite lumps. Images taken in transmitted light microscopy mode with crossed
870 polarizers.

871 Figure 4 Backscattered electron (BSE) images for the destinezite. (A) Equigranular
872 aggregate of destinezite (de-1) with thick hematite crystals displaying the typical
873 tabular/platy habit; both are affected by a fracture filled of supergene goethite. (B)

874 Aggregate of individual crystals of destinezite (de-2) exhibiting the pseudo-hexagonal
875 habit and the presence of abundant cleavage cracks along (100) as result of a
876 significant loss of water. Bleached zones (light gray) along the cleavage and fractures of
877 some crystals reveal variable transformation to secondary Fe-phosphate products. Black
878 zones are pore and cracks.

879 Figure 5 Thermal decomposition analysis of the El Laco destinezite under N₂-gas
880 atmosphere at a heating rate of 5°C/min. (A) Thermogravimetric curve TG (in blue) and
881 differential thermogravimetric curve DTG (in red); mass loss in percent and mass
882 derivative in %/°C, respectively. (B) Thermal decomposition for the destinezite (TG in
883 %), heat capacity (C_p, J/g°C), and associated enthalpy change (ΔH, J/g) in the
884 temperature range of 50 to 900°C.

885 Figure 6 Phase stability diagrams for the Fe-P-S-O system calculated using the Act2
886 application with GWB (Bethke, 2005) to illustrate the transformation of lipscombite to
887 destinezite in low-temperature hydrothermal conditions. The restrictions imposed are
888 those typical of the steam-heated environment, assuming geochemically reasonable
889 ranges of concentrations of dissolved species: activities of Fe²⁺, K⁺, and Ca²⁺ are set at
890 10⁻², while for SO₄²⁻ and HPO₄²⁻ the activity value vary according the model. Red solid
891 and dashed lines define the boundary separating the domains of the stable phases. The
892 open and cross-hatched circular areas represent the proposed initial (1) and final (2)
893 conditions for the transformation of lipscombite to destinezite. (A) Plot of stability fields of
894 iron phosphate, sulphate, and oxide in terms of variable dissolved total phosphate and
895 pH. The above imposed constraints to define the field boundaries include a SO₄²⁻ activity
896 of 10⁻², and oxidizing conditions. The upper half of the diagram illustrates the significant

897 reduction of the stability field of lipscombite with decreasing temperature. Dashed-lines
898 correspond to boundaries of stability field at 200 and 100°C. The plot of lower part of the
899 diagram shows the stable destinezite-hematite equilibrium at low temperature (100°C).
900 Blue dashed line is for the apatite-fluorite boundary at 300°C. Arrows indicate the
901 presumable trend followed by the fluids for the transformation of lipscombite to
902 destinezite and for fluorite precipitation. (B) Stability relationship between the three
903 identified phases (destinezite, lipscombite, and hematite) in aqueous solutions at
904 temperature of 100°C and variable pH (2, 3, and 4). Note the enlargement of the
905 destinezite field as the pH decreases in conformity with environments dominated by
906 acid-sulfate hydrothermal alteration. (C) Temperature-pH diagram for the main minerals
907 found in the destinezite lumps. Activities of iron and sulfur are the same as in (A). Note
908 the significant reduction of the stability field of lipscombite when the activity of HPO_4^{2-}
909 decreases from 10^{-3} to 10^{-5} . (D) Activity-pH diagram for the $\text{K}_2\text{O}-\text{Al}_2\text{O}_3-\text{SiO}_2-\text{P}_2\text{O}_5-\text{H}_2\text{O}$
910 system calculated at 100°C showing the stability of variscite relative to alunite, kaolinite,
911 muscovite, and K-feldspar; the dashed line correspond to the destinezite-hematite
912 boundary showed in lower half of the (A) diagram.

913

914 TABLES

915 **Table 1** Mineral chemical groups, names, and formulae for minerals cited in this study

916 **Table 2** Average microprobe analysis (wt %) of the El Laco destinezite and lipscombite
917 remnants from different lumps. For comparison, some published results of
918 destinezite/diadochite are included.

919 *(text to place at the bottom of this table2)*

920 Columns: (1) destinezite (this study; average of 40 analyses); (2) theoretical composition
921 of destinezite; (3) “diadochite” from El Laco ([Lledó, 2005](#)); average of 4 analyses by wet-
922 chemical method; (4) destinezite from Alum Cave Bluff, Tennessee USA ([Peacor et al.,](#)
923 [1995](#)); (5) destinezite from the Hinomaru-Nako mine, Japan (Matsubara et al., (1999); (6)
924 destinezite from Haut-le-Bastia, Belgium ([Anthony et al., 2005](#)); (7) diadochite from
925 Kurama Ridge, Urbekistan ([Moiseeva, 1967](#)); (8) lipscombite from remnants within the
926 lumps (this study, average of 14 analyses); (9) theoretical composition of lipscombite; the
927 amounts of FeO and Fe₂O₃ were calculated according the Fe²⁺/Fe³⁺ ratio of 1:2
928 ([Yakubovich et al., 2006](#)). The H₂O content of destinezite and lipscombite were
929 determined by difference, and apfu on the basis of 15 and 10 oxygens, respectively; (*)
930 water loss during wet chemical analysis; (#) water calculated by the Penfield method.
931 Rem. Amount of contaminants (mainly MgO, MnO, SrO, Na₂O, K₂O, usually below
932 detection limits). n.d. Not detected.

933 **Table 3** Variation of the enthalpy (ΔH in J/g) of the different stages of decomposition of
934 El Laco destinezite during the heating. DSC values determined in atmosphere of
935 nitrogen.

936 **Table 4** Thermodynamic properties for the products and reactants involved in the
937 calorimetric assays and calculated values for the El Laco destinezite.

938

939

940

Table 1

Group	Mineral name	Mineral formula
Oxides anion -O ²⁻	Goethite	Fe ³⁺ O(OH)
	Hematite	αFe ₂ O ₃
	Maghemite	γFe ₂ O ₃
	Magnetite	Fe ₃ O ₄
Phosphates anion -PO ₄ ³⁻	Apatite	Ca ₅ (PO ₄) ₃ (F,Cl,OH)
	Barbosallite	Fe ²⁺ Fe ³⁺ ₂ (PO ₄) ₂ (OH) ₂
	Beraunite	Fe ²⁺ Fe ³⁺ ₅ (PO ₄) ₄ (OH) ₅ •4H ₂ O
	Cacoxenite	(Fe ³⁺ Al) ₂₅ (PO ₄) ₁₇ O ₆ (OH) ₁₂ •75H ₂ O
	Crandallite	CaAl ₃ (PO ₄) ₂ (OH) ₅ •H ₂ O
	Delvauxite	CaFe ³⁺ ₄ (PO ₄ ,SO ₄) ₂ (OH) ₈ •4-6(H ₂ O)
	Dufrénite	Fe ²⁺ Fe ³⁺ ₄ (PO ₄) ₃ (OH) ₅ •2H ₂ O
	Giniite	Fe ²⁺ Fe ³⁺ ₄ (PO ₄) ₄ (OH) ₂ •2H ₂ O
	Grattarolaite	Fe ³⁺ ₃ PO ₄ O ₃
	Heterosite	Fe ³⁺ PO ₄
	Lipscombite	Fe ²⁺ Fe ³⁺ ₂ (PO ₄) ₂ (OH) ₂
	Monazite	(La,Ce,Nd)PO ₄
	Phosphoferrite	(Fe ²⁺ ,Mn) ₃ (PO ₄) ₂ •3H ₂ O
	Phosphosiderite	Fe ³⁺ PO ₄ •2H ₂ O
	Rockbridgeite	Fe ³⁺ ₅ (PO ₄) ₃ (OH) ₅
	Rodolicoite	Fe ³⁺ PO ₄
	Strengite	Fe ³⁺ PO ₄ •2H ₂ O
	Tinticite	Fe ³⁺ ₅ (PO ₄ ,VO ₄) ₄ •7H ₂ O
Variscite	AlPO ₄ •2H ₂ O	
Vivianite	Fe ²⁺ ₃ (PO ₄) ₂ •8H ₂ O	
Sulfate-phosphates anions -SO ₄ ²⁻ , -PO ₄ ³⁻	Destinezite	Fe ³⁺ ₂ (PO ₄)(SO ₄)(OH)•6H ₂ O
	Diadochite	Fe ³⁺ ₂ (PO ₄)(SO ₄)(OH)•6H ₂ O
	Svanbergite	SrAl ₃ (PO ₄)(SO ₄)(OH) ₆
	Woodhouseite	CaAl ₃ (PO ₄)(SO ₄)(OH) ₆
Sulfates anion -SO ₄ ²⁻	Alunite	KAl ₃ (SO ₄) ₂ (OH) ₆
	Anhydrite	CaSO ₄
	Gypsum	CaSO ₄ •2H ₂ O
	Jarosite	KFe ³⁺ ₃ (SO ₄) ₂ (OH) ₆
	Melanterite	Fe ³⁺ SO ₄ •7H ₂ O
	Mikasaite	Fe ³⁺ ₂ (SO ₄) ₃
Sulfides	Chalcopyrite	CuFeS

anion -S ²⁻	Pyrite	FeS ₂
Silicates anion -Si _x O _y	Kaolinite K-feldspar Muscovite Plagioclase Quartz Smectite Tridymite	Al ₂ Si ₂ O ₅ (OH) ₄ (K,Na)(Si,Al) ₄ O ₈ KAl ₂ (Si ₃ Al)O ₁₀ (OH,F) ₂ (Na,Ca)(Si,Al) ₄ O ₈ SiO ₂ (Na,Ca) _{0,3} (Al,Mg) ₂ Si ₄ O ₁₀ (OH) ₂ •n(H ₂ O) SiO ₂
Halides anion -F ¹⁻	Fluorite	CaF ₂

Table 2

	Destinezite			Destinezite/diadochite from the literature				
	1		2	3		4	5	6
	wt%	StdDev	wt%	wt%	StdDev	wt%	wt%	wt%
P2O5	18.35	0.96	16.59	22.15	0.19	17.10	17.06	16.83
SO3	17.41	1.58	18.71	15.94	0.58	20.70	19.78	17.21
FeO(t)	34.89	1.90	35.59			32.57	34.61	34.01
Fe2O3*	38.77		37.33	47.70	1.19	36.20	38.46	37.80
FeO*				0.86	0.02			
CaO	0.44	0.17	n.d.	0.57	0.40	n.d.	n.d.	n.d.
SiO2	0.50	0.18	n.d.	0.28	0.12	n.d.	n.d.	n.d.
Al2O3	0.22	0.30	n.d.	n.d.		2.70	0.33	n.d.
MgO	0.04	0.06	n.d.	0.04	0.02	0.30	n.d.	n.d.
MnO	0.01	0.01	n.d.	n.d.		n.d.	n.d.	n.d.
Rem.				1.00				0.89
H2O	24.26		27.37	10.21(*)	0.74	23.00	24.37	26.8(#)
Total	100.00		100.00	97.89		100.00	100.00	72.73
	Number of ions on the basis of 15 oxygens							
P	1.14	0.15	1.00	1.64	0.01	1.06		1.04
S	0.96	0.11	1.00	1.05	1.04	1.14		0.94
Fe ³⁺	2.14	0.26	2.00	3.08	0.10	1.99		2.07
Fe ²⁺				0.06	0.00	0.08		
Ca	0.03	0.02		0.05	0.04			
Al	0.01	0.04				0.17		
Mg	0.00	0.00		0.00	0.00			
Mn	0.00	0.00						
OH	1.00		1.00	1.00		1.00		1.00
H2O	5.43		6.00	2.48		5.11		6.00

Lipscombite			
7	8		9
wt%	wt%	StdDev	wt%
15.92	36.26	1.15	36.26
19.16	0.20	0.21	n.d.
34.84	53.60	1.14	55.05
38.72	39.91		40.79
	17.69		18.35
n.d.	0.64	0.50	0.00
n.d.	0.63	0.19	0.00
0.72	0.25	0.19	0.00
n.d.	0.06	0.40	n.d.
n.d.	0.33	0.90	n.d.
0.69			n.d.
24.68	4.66		4.60
99.89	100.00		100.00
Ions on the basis of 10 oxygens			
0.99	1.99	0.29	2.00
1.06	0.01	0.00	
2.14	1.94	0.26	2.00
	0.97	0.13	1.00
	0.04	0.07	
0.05	0.01	0.00	
	0.00	0.00	
	0.01	0.00	
1.00	2.02		2.00
5.55			

Table 3

Step	T _i (°C)	T _f (°C)	%mass loss	ΔH _{associated} (J/g)	Assignment
1	50	115	9.4	210	1rst partial dehydration: 2·H ₂ O
2	115	166	9.1		2nd partial dehydration: 2·H ₂ O
3	165	350	12.0	315	Complete' dehydration and formation of lipscombite, Fe ²⁺ Fe ³⁺ 2(PO4)2(OH)2; begin the formation of mikasaite and amorph iron phosphate hydroxide
4	350	594		58	
5	594	648	1.7	539	Partial dehydration of lipscombite and formation of mikasaite plus iron phosphate
6	648	725	9.9		Partial dehydration and desulfurization with formation of grattarolaite Fe ₃ (PO ₄)O ₃ and iron phosphate Fe ₄ (P ₄ O ₁₂) ₃ ; decomposition of mikasaite
7	725	900	3.0		Complete decomposition of limpscombite and mikasaite (desulfuration) and formation of hematite, grattarolaite, and rodolicoite

Table 4

Formula	Min. Name	DfH°	DfS°	DfG°
		(KJ/mol)	(J/mol.K)	(KJ/mol)
Fe ²⁺		-92.257	-2.456	-91.525
SO ₄ ²⁻		-909.602	-554.219	-774.362
HPO ₄ ²⁻		-1292.082	-680.884	-1089.076
SO ₂ (g)		-296.81	11.00	-300.09
H ₂ O(g)		-241.83	-44.42	-228.58
Fe ₃ (PO ₄) ₃	Grattarolaite	-2097.92	-1024.63	-1930.04
Fe(PO ₄)	Rodolicoite	-1297.00	-384.95	-1182.23
Fe ₂ O ₃	Hematite	-823.00	-274.88	-741.04
Fe ₂ (SO ₄)(PO ₄)(OH).6H ₂ O	Destinezite	-4051.70	-1518.47	-3598.98
Fe ₂ (SO ₄)(PO ₄)(OH).6H ₂ O	Destinezite	-3928.16		-3570.00
Fe ₂ (SO ₄)(PO ₄)(OH).6H ₂ O	Destinezite	-3999.45		-3425.27

Source
HSC database (Roine, 2002)
HSC database (Roine, 2002)
HSC database (Roine, 2002)
HSC database (Roine, 2002)
HSC database (Roine, 2002)
Values estimated by applying the method of addition of oxide units (Fe as trivalent) (La Iglesia, 2009)
HSC database (Roine, 2002)
HSC database (Roine, 2002)

This study: experimental
Values obtained according the method of La Iglesia (2009)
Values obtained following the ideal mixing method (Nriagu & Dell 1974; Gaskova, 2008)

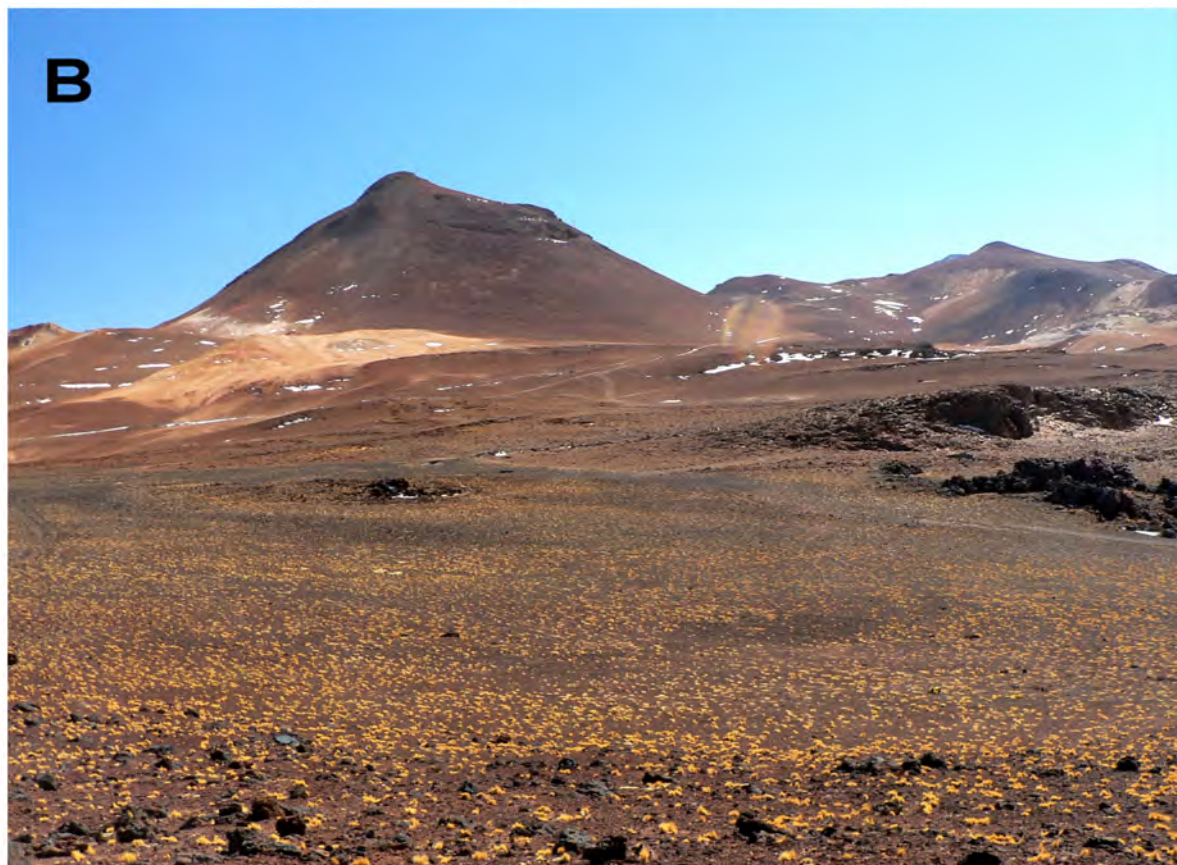
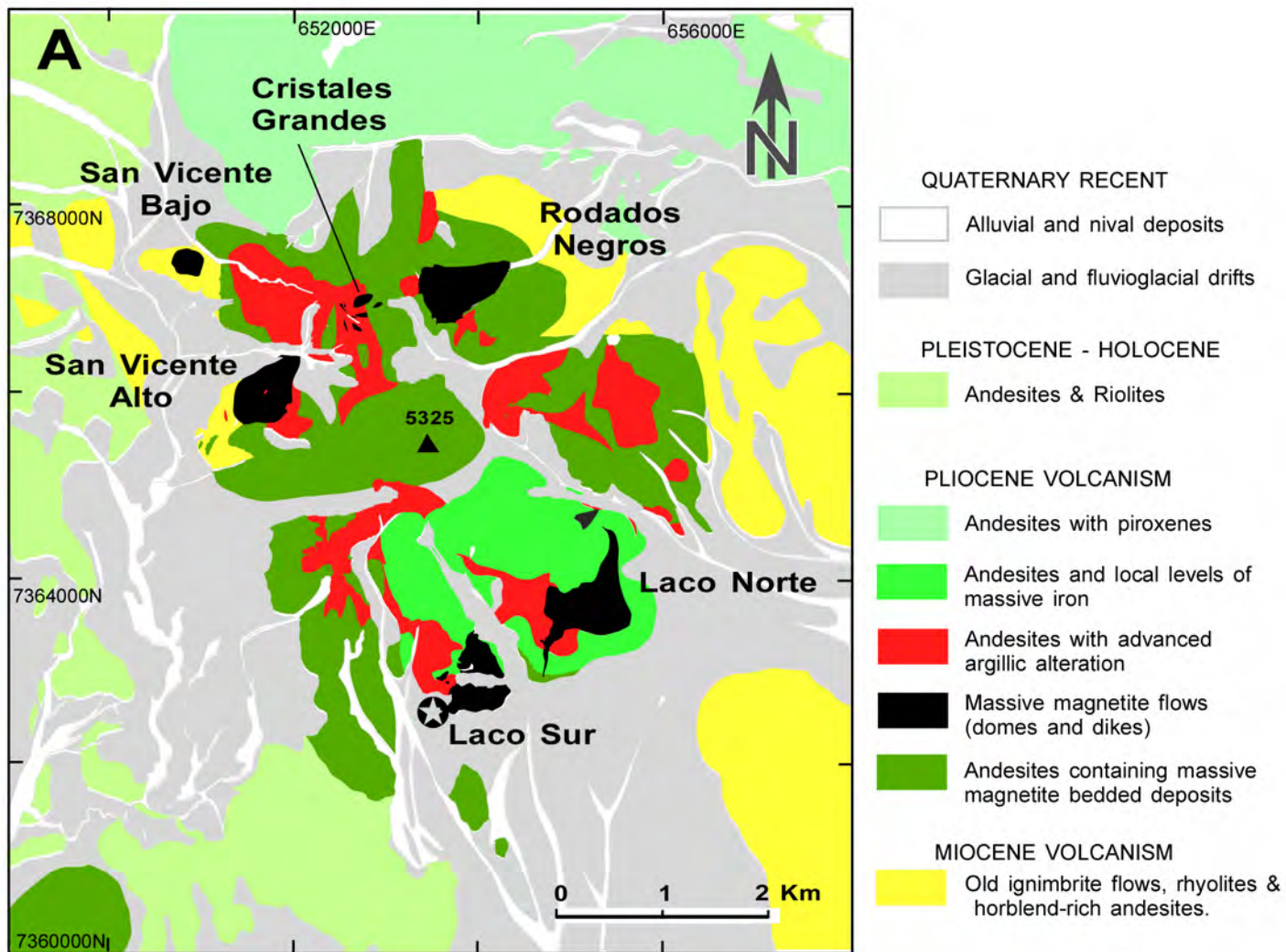


Fig 1



Fig 2

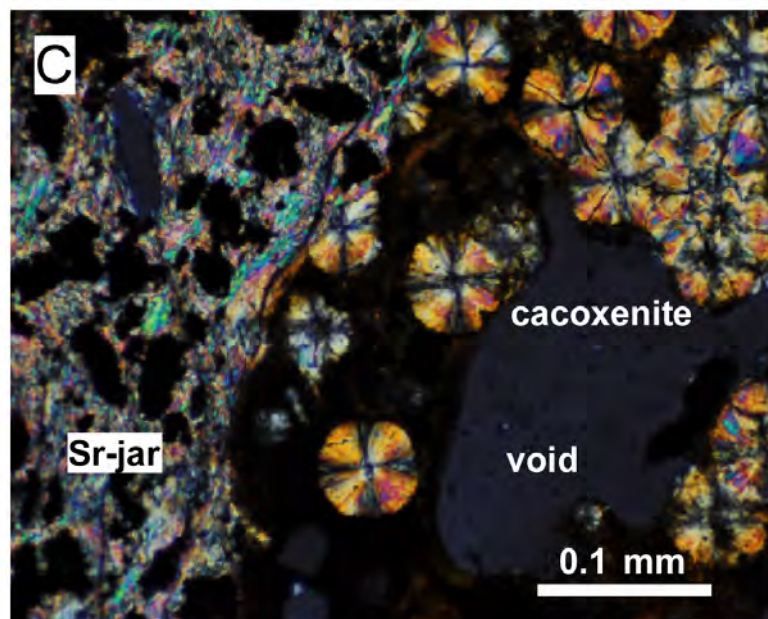
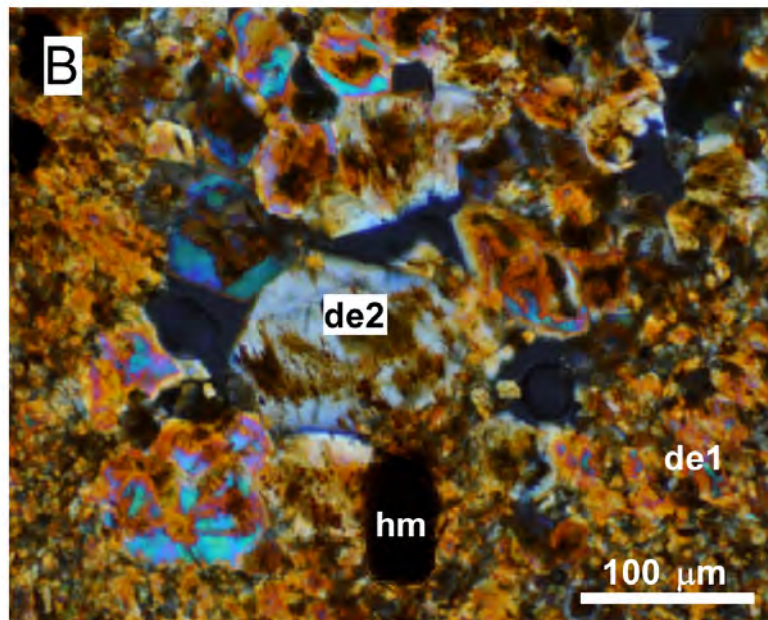
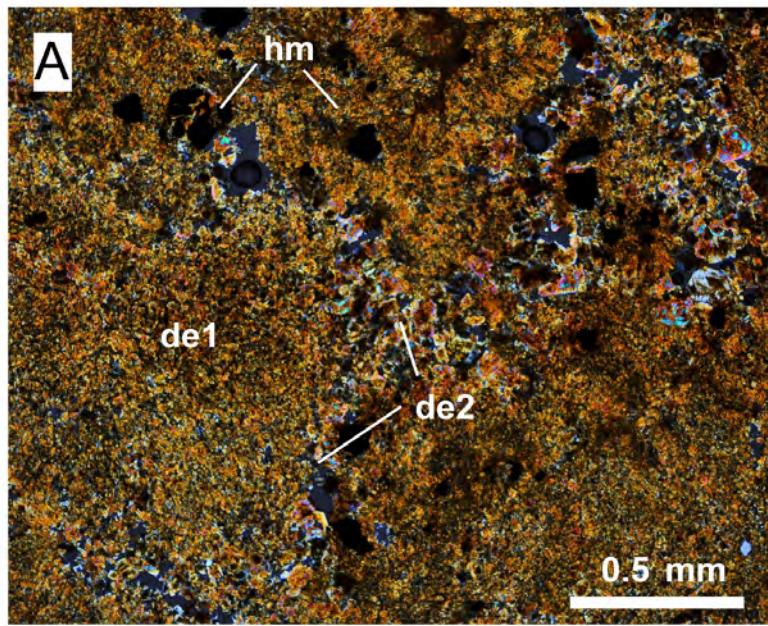


Fig 3

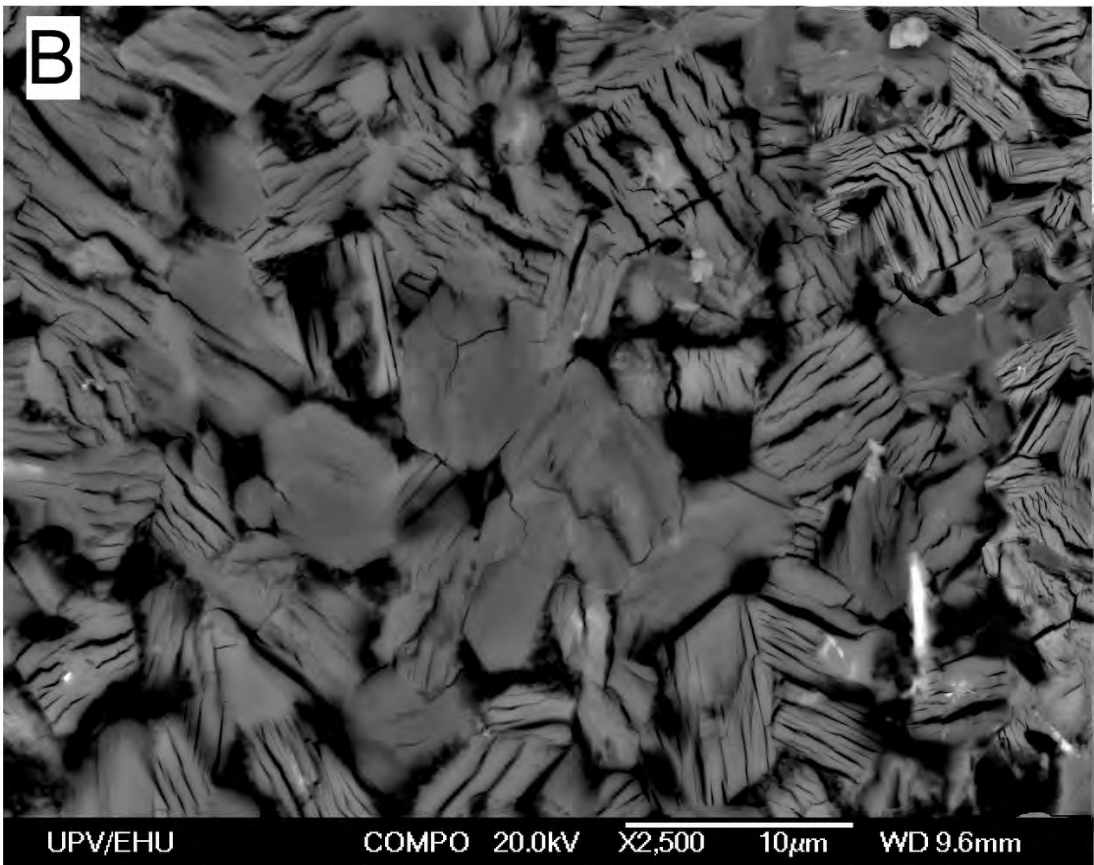
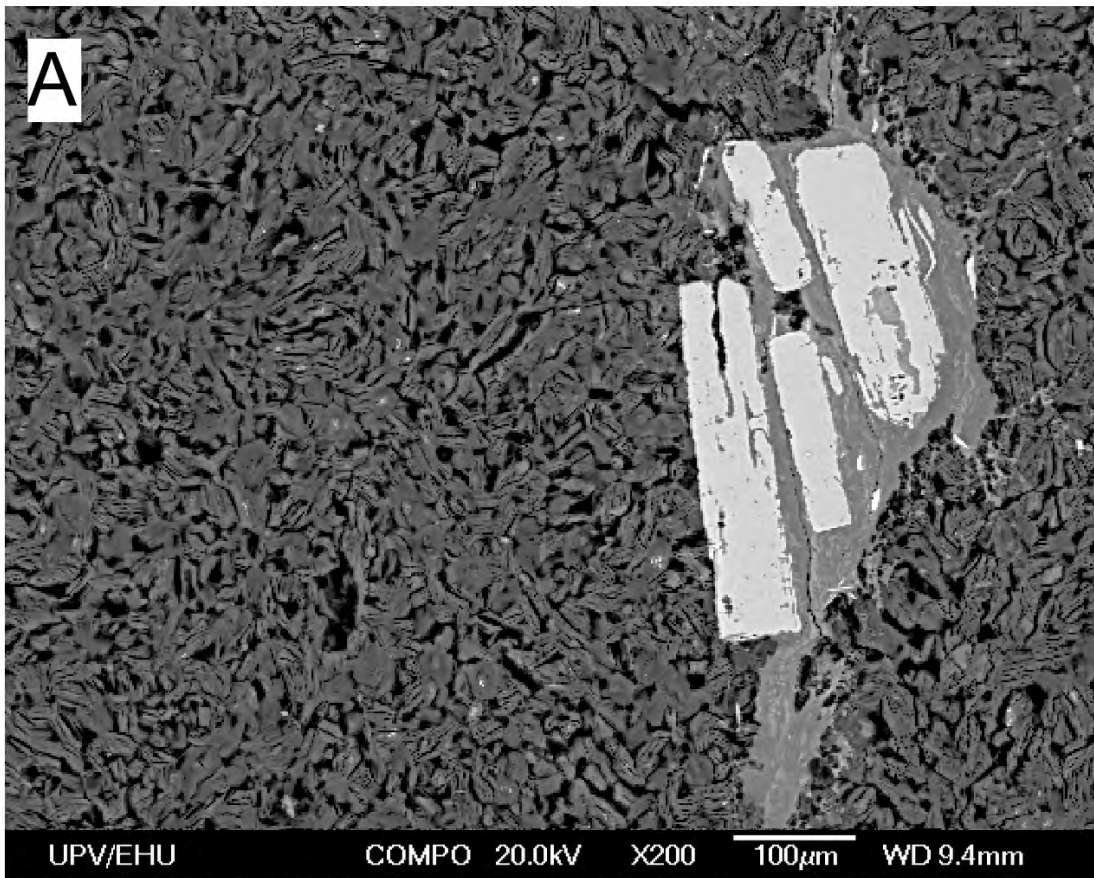


Fig 4

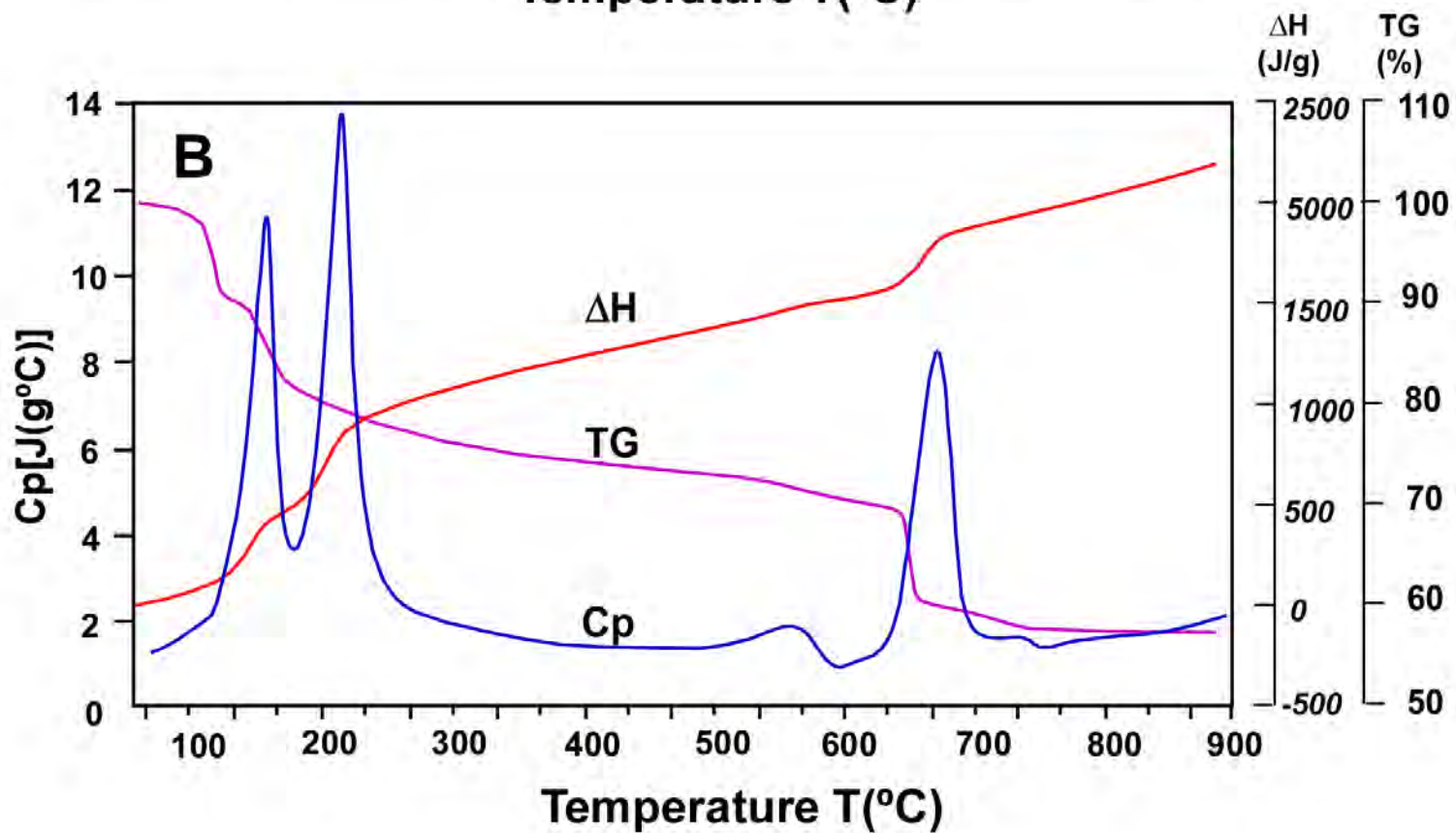
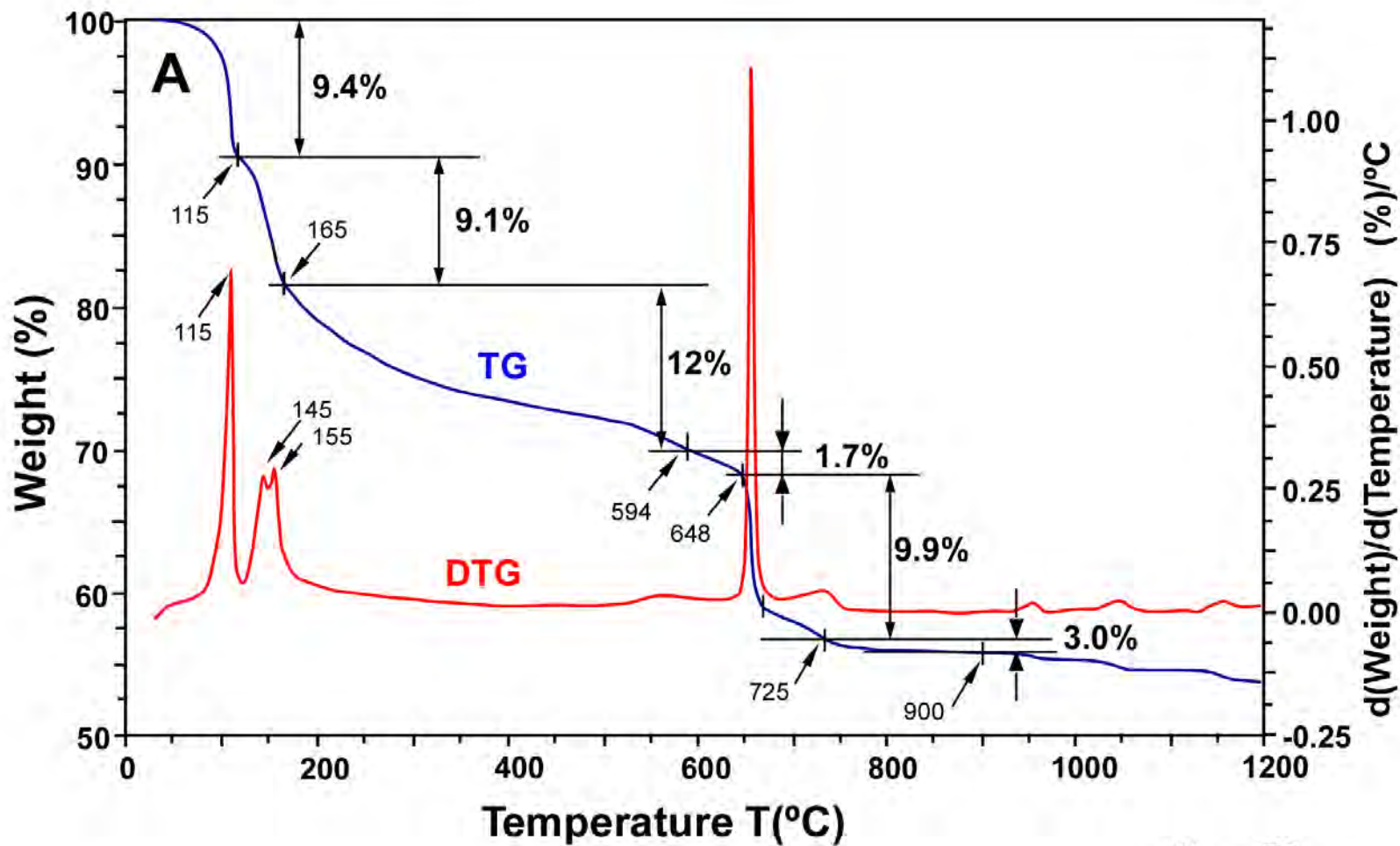


Fig 5

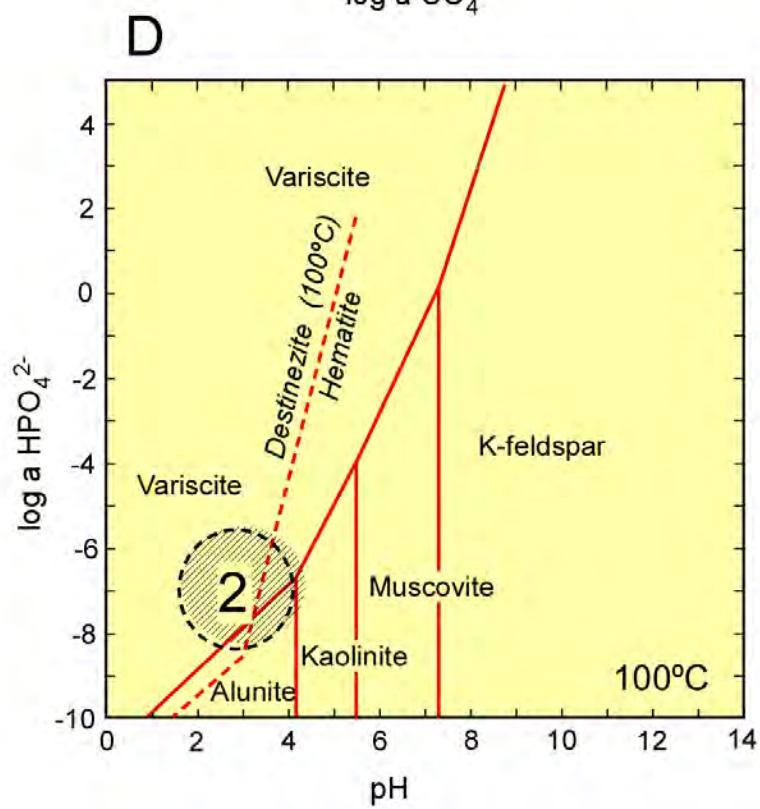
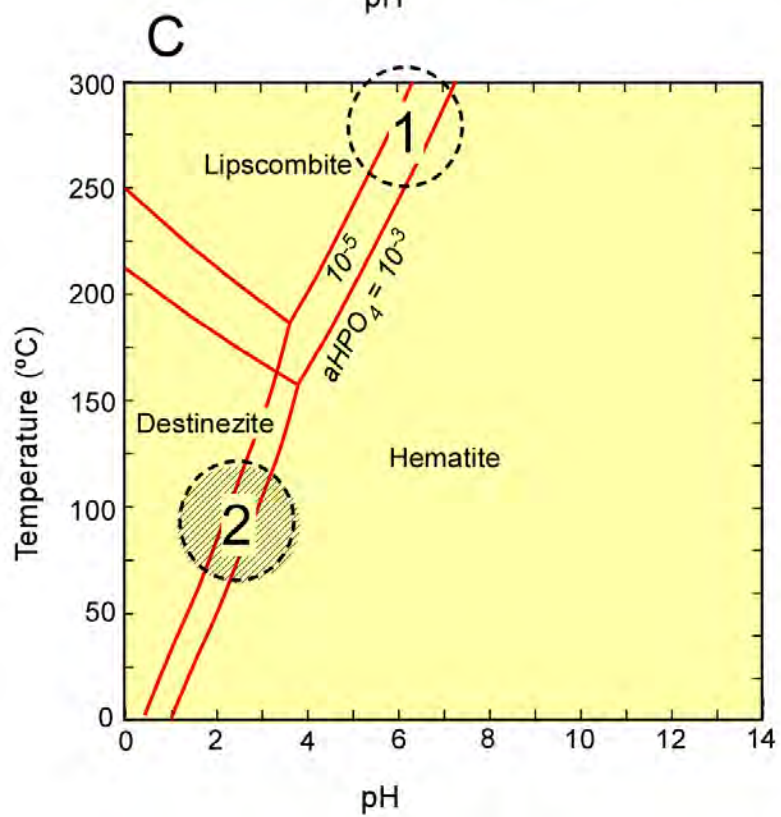
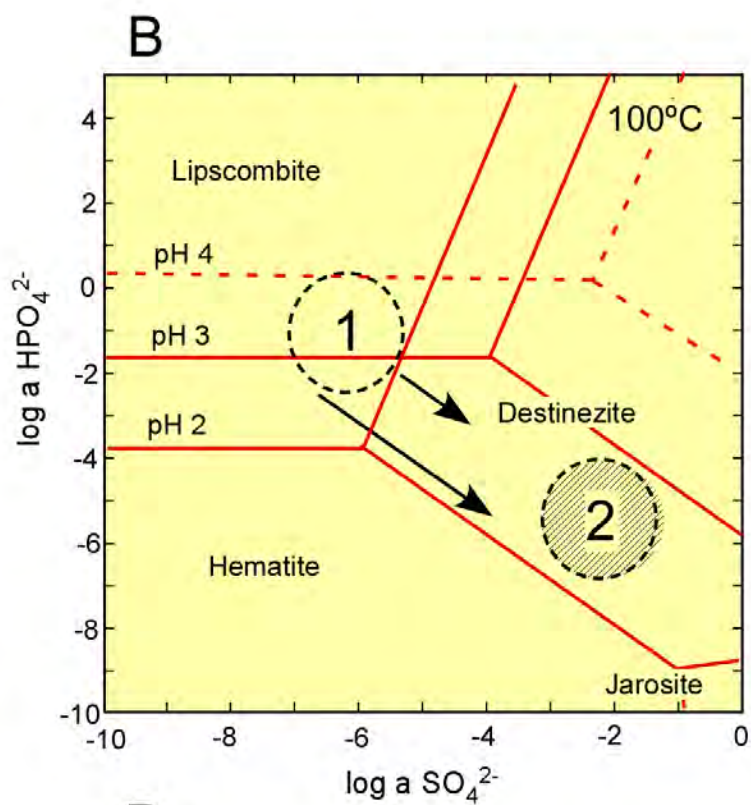
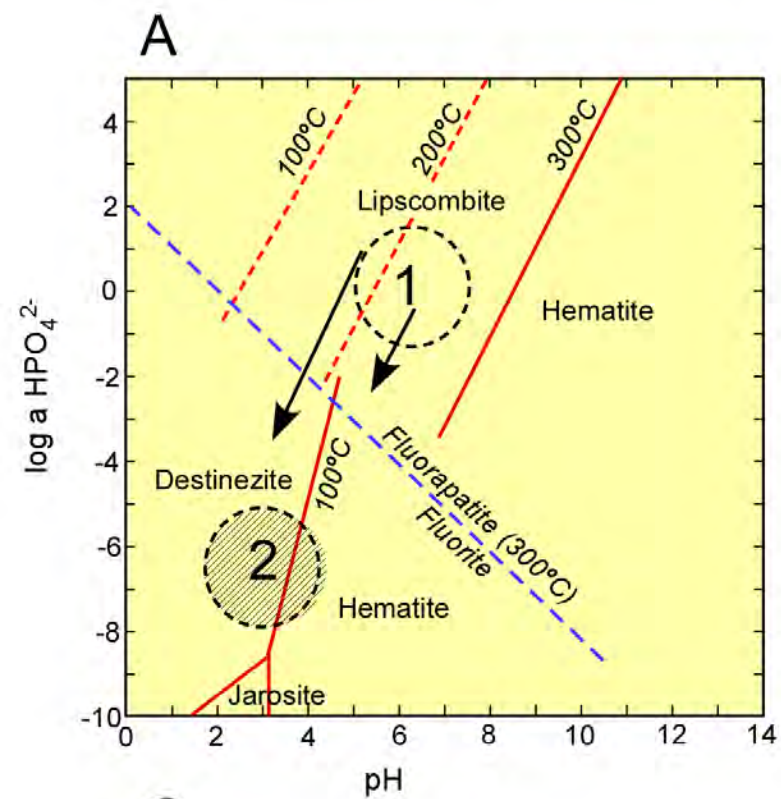


Fig 6